




The role of breakup and coalescence in fine-scale bubble-induced turbulence. I. Dynamics


Cite as: Phys. Fluids **34**, 083321 (2022); <https://doi.org/10.1063/5.0094573>


Submitted: 04 April 2022 • Accepted: 23 May 2022 • Accepted Manuscript Online: 04 August 2022 • Published Online: 29 August 2022

Published open access through an agreement with Newcastle University

 I. Paul,  B. Fraga,  M. S. Dodd, et al.

COLLECTIONS

 This paper was selected as Featured

 This paper was selected as Scilight



View Online



Export Citation



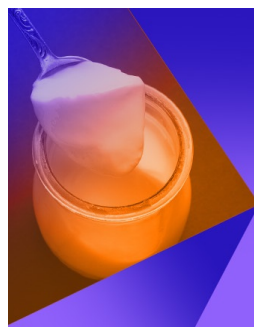
CrossMark

ARTICLES YOU MAY BE INTERESTED IN

The role of breakup and coalescence in fine-scale bubble-induced turbulence. II. Kinematics
Physics of Fluids **34**, 083322 (2022); <https://doi.org/10.1063/5.0100334>

Bubbles generate their own kind of turbulence
Scilight **2022**, 361103 (2022); <https://doi.org/10.1063/10.0013892>

Multiscale analysis of the Reynolds stress, dissipation, and subgrid-scale tensor in turbulent bubbly channel flows: Characterization of anisotropy and modeling implications
Physics of Fluids **34**, 085122 (2022); <https://doi.org/10.1063/5.0104594>



Physics of Fluids

Special Topic: Food Physics

Submit Today!

The role of breakup and coalescence in fine-scale bubble-induced turbulence. I. Dynamics



Cite as: Phys. Fluids **34**, 083321 (2022); doi: [10.1063/5.0094573](https://doi.org/10.1063/5.0094573)

Submitted: 4 April 2022 · Accepted: 23 May 2022 ·

Published Online: 29 August 2022



View Online



Export Citation



CrossMark

I. Paul,^{1,a)} B. Fraga,² M. S. Dodd,³ and C. C. K. Lai⁴

AFFILIATIONS

¹School of Engineering, Newcastle University, Newcastle upon Tyne NE1 7RU, United Kingdom

²School of Engineering, University of Birmingham, Birmingham B15 2TT, United Kingdom

³Center for Turbulence Research, Stanford University, Stanford, California 94306, USA

⁴School of Civil and Environmental Engineering, Georgia Institute of Technology, Atlanta, Georgia 30332, USA

^{a)} Author to whom correspondence should be addressed: immanuvel.paul@newcastle.ac.uk

ABSTRACT

We study the effect of bubble breakup and coalescence on fine-scale dynamics of bubbly turbulent flows using direct numerical simulations. We perform two different simulations of dilute bubbly flows of void fraction 0.5%: one with bubbles breaking up and coalescing and the other without these physical processes. The volume of the fluid method is used for simulating bubbles undergoing breakup and coalescence while the bubbles are treated as rigid spheres in the immersed boundary method simulation. The energy spectrum in both types of simulation, consistent with previous studies, exhibits a -3 slope. We follow a single infinitesimal fluid element as it evolves to understand velocity gradient dynamics using conditional mean trajectories. We note finite-time divergence when the fluid element evolves under the action of inertial and pressure dynamics. The inertial, pressure, and viscous velocity gradient dynamics, when considered individually, produce the same results for bubble-induced turbulence (BIT) as with the classical homogeneous isotropic turbulence (HIT). Yet when the overall velocity gradient dynamics is considered, BIT results in non-cyclic trajectories moving toward stable node and unstable saddle while classical HIT shows cyclic behavior in their trajectories that move toward the origin. Interestingly, both the volume of fluid and immersed boundary simulations produce similar results. Therefore, there are two main takeaways from this research. First, new velocity gradient models are needed for BIT as their velocity gradients behavior is entirely different from the HIT. Second, we can neglect the bubble topology, breakup, and coalescence while studying or modeling the fine-scale dynamics of BIT.

© 2022 Author(s). All article content, except where otherwise noted, is licensed under a Creative Commons Attribution (CC BY) license (<http://creativecommons.org/licenses/by/4.0/>). <https://doi.org/10.1063/5.0094573>

I. INTRODUCTION

Turbulent bubbly flows are common both in nature and in industry.^{1–3} Ocean waves and mist contain air bubbles that affect the transport properties of the liquid continuous phase. Many industrial applications, such as distillation, absorption, flotation, spray drying, electro-machining, and boiling involve bubbly flows.⁴ Unlike single-phase flows that often require an external pressure gradient for the flow to happen, the bubbly flows that we consider in this paper can happen entirely due to buoyancy alone. That is, the bubbles rise due to the differences in densities of the dispersed bubble phase and the liquid continuous phase. When a bubble rises due to buoyancy, it causes velocity fluctuations to the surrounding liquid and this is often called bubble induced turbulence (BIT).¹

Lance and Bataille,⁵ in their pioneering work, performed experiments of a homogeneous swarm of bubbles in the presence of a

turbulence-generating grid. They found that increasing the void fraction (α) increases the turbulent kinetic energy of BIT. They also reported that, as the void fraction increases, the one-dimensional energy spectra of the liquid phase slowly changes from a $-5/3$ slope to a near -3 slope. Ever since this study, there have been various experimental studies conducted on this configuration.^{6–13} These experimental studies have revealed many of the characteristics of bubble-induced velocity fluctuations. Many studies have proven that the intensity of bubble-induced fluctuation increases with bubble concentration or void fraction.^{5,8} Risso and Ellingsen⁷ showed that these velocity fluctuations are controlled by interactions of bubble wakes. Much of the velocity fluctuations are generated in the close region surrounding the bubble, and the magnitude of these fluctuations decreases as we move away from the bubble into the far wake region. While these velocity fluctuations are independent of void fraction in the near wake region

of the bubble, there is some dependency in the far-wake region. Risso and Ellingsen⁷ arrived at scaling for probability density distributions (PDF) of these velocity fluctuations in the far-wake, which scale with the void fraction as $\alpha^{0.4}$. Riboux *et al.*⁹ obtained scaling laws for the largest and smallest length scales in BIT in terms of problem parameters such as the void fraction. These experiments also show that the PDFs of these velocity fluctuations are non-Gaussian in the direction along which the bubble moves. The magnitude of such velocity fluctuations along the bubble moving direction is found to be higher than the fluctuations along the other directions.

As mentioned before, the other important result in BIT is the observation of a -3 slope in the energy spectrum.^{5,8,9,11} This observation clearly shows that the characteristic of BIT is different from the classical homogeneous isotropic turbulence (HIT). It is generally believed that the localized disturbances due to the bubble movement give rise to this phenomenon.¹⁴

Bunner and Tryggvason¹⁵ pioneered the numerical modeling of bubbly flows for low Reynolds numbers. Following their study, there are many numerical studies on this problem.^{16–21} These studies have corroborated the important experimental observations such as the -3 slope in the energy spectrum and the non-Gaussian behavior of the velocity fluctuations PDFs.^{16,18} Moreover, the numerical studies have identified a bubble-free wall layer in a bubbly pipe flow and the corresponding mechanism through which the bubbles move in and out of the wall layer.^{17,20} Very recent numerical studies shed light on the energy cascade mechanism behind the -3 energy spectrum slope through the spectral scale-by-scale energy transport analysis.^{22–24} There are also various studies on the application of bubbly flows in drag reduction, polymers, swirl atomizer, and oxygen transfer in atmosphere.^{25–29}

According to Tsinober,³⁰ the large-scale terms of turbulence are represented by velocity fluctuations while the turbulent small-scale terms are written in terms of velocity gradients. Going with this definition, we see from the BIT literature that most of the studies have focused only on the large-scale aspect of BIT. We know that the large scales in turbulent flows are often dictated by the boundary conditions of the problem, and their properties vary from one problem to another. On the contrary, the small scales of turbulence are unaffected by the problem parameters and any universal turbulence theory can be developed only based on fine-scale turbulence. There are two ways to analyze the small scales of turbulence. In the first method, the small scales are studied for their statistical behavior in terms of their PDFs and joint probability functions (JPDF). Such a study is commonly called topological studies as they reveal the topology of fine-scale turbulence. In the second method, we track a fluid element for its velocity gradient to see how it reacts to various forces acting on the element. This study is called the dynamical study of fine-scale turbulence.

Looking at the BIT literature, we see that there is no experimental study that focuses on fine-scale BIT. Very recently, there has been a few direct numerical simulation (DNS) studies on the topological aspects of small-scale BIT.^{31–34} These studies are further examined in the second part of this work. Yet, to the best of our knowledge, there are no studies available on the dynamical aspect of BIT. Martin *et al.*³⁵ and Ooi *et al.*³⁶ studied the dynamical aspect for HIT. It is well known from their studies that the movement of a fluid element in the phase map of the second and third velocity gradient is cyclic. Following these works, similar studies have been carried out on various turbulent systems.^{37,38} No such study, however, is available in the literature for BIT.

This warrants a detailed study on this aspect. Above all, previous studies have shown the effectiveness of BIT in mixing and heat transfer^{39–41} and we know that diffusion takes place due to the action of turbulent small scales. This means that a study on the dynamical aspect of fine-scale BIT would help to develop universal theories of BIT. Therefore, we study BIT for a periodic bubbly column using high-resolution DNS.

We ask the following two questions in this study. First, what is the impact of bubble breakup and coalescence on the dynamical aspect of fine-scale BIT? Second, how does BIT compare with the classical HIT when it comes to the dynamical characteristics of fine-scale turbulence? To answer these questions, we carry out bubbly turbulent flow in a vertical column using two different numerical techniques. First, we use the volume of fluid (VoF) method, which models the bubble breakup and coalescence. Second, we also simulate the same system using an Eulerian–Lagrangian immersed boundary method (IBM) where the bubbles do not undergo breakup and coalescence. To compare with the HIT and to gain confidence in the postprocessing tools we developed, we also simulate the HIT in a periodic box.

This paper is organized as follows. The governing equations along with the numerical methodologies are presented in Sec. II. Section III presents the numerical details of the simulations. The results are presented in Sec. IV, and Sec. V summarizes the main takeaways from this study.

II. GOVERNING EQUATIONS AND NUMERICAL METHODOLOGY

The dynamics of the continuous liquid matrix are predicted through direct numerical simulation (DNS) of the Navier–Stokes equations for an unsteady, incompressible and viscous flow, described by the following equations:

$$\nabla \cdot \mathbf{u} = 0, \quad (1a)$$

$$\frac{\partial \mathbf{u}}{\partial t} + \mathbf{u} \cdot \nabla \mathbf{u} = -\frac{1}{\rho} \nabla p + \nu \nabla^2 \mathbf{u} + \mathbf{f}, \quad (1b)$$

where $\mathbf{u} = \mathbf{u}(\mathbf{x}, t)$ is the fluid velocity, ρ is the density, $p = p(\mathbf{x}, t)$ is the scalar pressure field, ν is the water's kinematic viscosity, and $\mathbf{f} = \mathbf{f}(\mathbf{x}, t)$ is the body force term exerted at the bubble–liquid interface. We adopted two fundamentally different approaches to simulate the dispersed phase, which results in different ways of calculating \mathbf{f} . These equations are solved using the volume of fluid method (VoF) and the immersed boundary method (IBM). We also simulate Homogeneous Isotropic turbulence (HIT) in a periodic box. Details about these methodologies are presented in the Appendix.

III. COMPUTATIONAL DETAILS

A bubble swarm was simulated in a periodic vertical channel in which the bubble's buoyancy is the only source of motion. The channel's dimensions are $40D_0 \times 20D_0 \times 20D_0$, where D_0 is the initial bubble diameter. The periodic boundary condition for the continuous and discrete phases was applied in all directions, as shown in Fig. 1. The initial bubble diameter is $D_0 = 2$ mm, providing that $Re_p \approx 400$ and the gravity acceleration is $\mathbf{g} = -9.81 \text{ ms}^{-2}$. To prevent uniform acceleration of the gas–liquid flow in the VoF simulation, we explicitly account for the hydrostatic pressure term in the momentum equation by adding a body force opposing the acceleration due to gravity.⁴² For the VoF simulation, the Eötvös number based on the initial bubble diameter is $Eu = 0.538$ and it reaches to a maximum value of 13 for

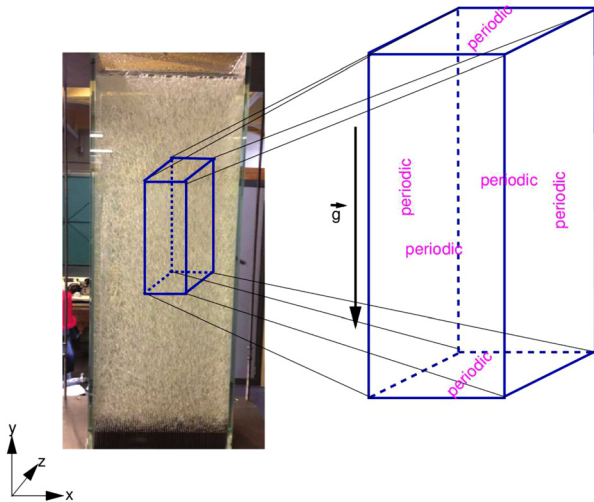


FIG. 1. Computational domain with boundary conditions.

the largest bubble size. Please note that the coordinate system shown in Fig. 1 is applicable for VoF simulation only as the gravity direction is taken as the x -axis for the IBM simulation. A void fraction of 0.5% was simulated for IBM and VoF. The grid resolution for VoF corresponds to approximately 13 grid points per initial bubble diameter, and for IBM, there are 8 Eulerian cells across the bubble diameter, yielding 210 Lagrangian markers per bubble. Further details about the simulations, mesh independence study, and validations can be found in our previous works.^{22,42–44}

For the case of HIT, we use a periodic box of size $2\pi \times 2\pi \times 2\pi$ with 128 mesh points along each direction. The Reynolds number based on the Taylor length scale (Re_λ) is 80 for the HIT case.

IV. RESULTS AND DISCUSSION

This section presents the main results of this study. We first present the evolution of turbulent kinetic energy (TKE) and energy

spectra at some specific time instants along with snapshots of the flow field to provide an idea of what sort of flow that we are dealing with. We also pick two locations based on these evolutions. Then, we discuss the velocity gradient dynamics for these two locations.

A. Evolution of turbulent kinetic energy and its spectra

Before we discuss the main results, it is helpful to remember that the number of bubbles and their size remains the same throughout the simulation in IBM as the bubbles do not undergo breakup and coalescence in the IBM simulation. In the VoF simulation, however, the bubbles break up and coalesce and, thus, the number of bubbles keeps decreasing during the simulation. The variation of the number of bubbles in the VoF simulation with respect to time is shown in Fig. 2(a). The breakup and coalescence of bubbles in VoF simulation also alter the bubble size distribution. This can be visualized from the result shown in Fig. 2(b) where D_{eq} is the equivalent sphere diameter.

Figure 3 depicts the temporal evolution of turbulent kinetic energy of the bubbly flows. Both VoF [Fig. 3(a)] and IBM [Fig. 3(b)] predict the same trend of TKE evolution. Since the bubbles are introduced in a quiescent fluid, there is no TKE at $t = 0$ in both simulations. Once the bubbles start rising in the channel, the TKE slowly increases irrespective of whether the bubbles break up and coalesce. It is generally believed that the turbulence here arises from two contributions.¹⁴ The first one is the disturbances due to bubble movements. The second one is the instability of the liquid that turns to turbulence beyond a certain critical Reynolds number. Therefore, both cases are in an unsteady state for a reasonable amount of time. This unsteady state could be attributed to the intermittent wake interactions between the vortices shed by the individual bubbles in the bubble wakes. Once the bubble wakes are fully mixed, we start to observe a quasi-steady state in both simulations. In IBM, this quasi-steady state is entirely due to the homogeneous mixing of the bubble wakes as the number of bubbles remain the same throughout the simulation. In VoF, however, the number of bubbles continues to decrease due to breakup and coalescence until the bubbles reach their terminal velocity. Therefore, when the effect of breakup and coalescence is present, the quasi-steady state is marked by a reduced yet constant number of bubbles whose velocities are comparable to the terminal velocity. Here, the amount of

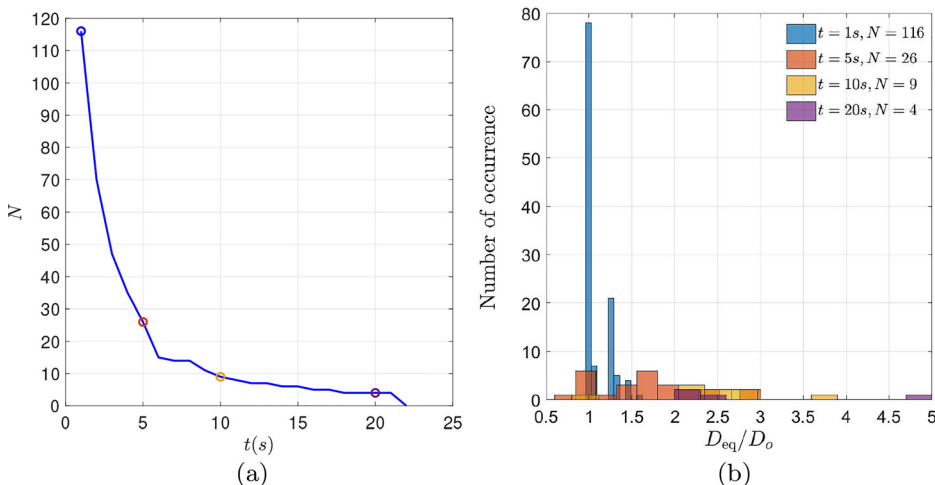


FIG. 2. (a) Number of bubbles over time. (b) Bubble size distribution in VoF simulation.

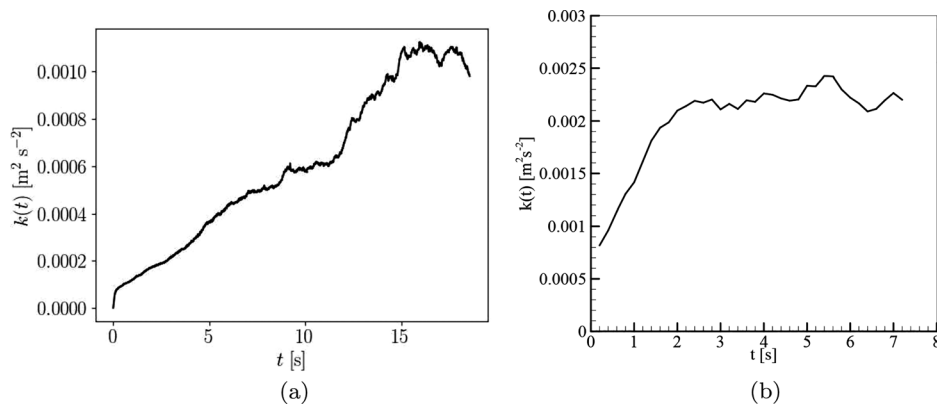


FIG. 3. Temporal evolution of turbulent kinetic energy obtained using (a) VoF and (b) IBM.

intermittent wake interaction continues to exist even in the quasi-steady state albeit the level of intermittency is low compared to the unsteady state.

Having discussed the TKE evolution, now we turn our attention to the energy spectra. It is easy to compute the spectra of TKE for single-phase flows, but it is not straightforward for bubbly flows as the velocity signals are discontinuous. The literature shows that there are mainly three ways to circumvent this problem.¹ Yet, all the methods result in the same conclusion that the spectrum of turbulent kinetic energy has a k^{-3} slope, where k is the wavenumber. In some studies, a $-5/3$ slope was also present at high wavenumbers. This is attributed to the fact that those studies also had shear-induced turbulence (for instance, grid-generated turbulence) besides the bubbly flows. Therefore, such studies designated a -3 slope for bubble-induced turbulence and a $-5/3$ slope for the shear-induced turbulence.

In this study, we consider only the velocity signal of the continuous phase by avoiding the bubble phase. Since the flow is temporally developing, as noted in Fig. 3, it is reasonable to look when exactly the energy spectra starts exhibiting the best possible -3 wavelength range. Figure 4 shows the energy spectra in the unsteady region where the energy spectrum starts exhibiting the best -3 slope. We call this location US_{-3} , where US stands for unsteady and -3 represents the slope of the energy spectrum at that location. The red, blue and green lines in Fig. 4 correspond to fluctuations along x , y , and z directions, respectively. We have normalized the TKE with root mean square (rms) values of velocity fluctuations corresponding to the particular direction. We have also put the experimental data of Riboux *et al.*⁹ as dotted lines in the same figure. Figure 4 corresponds to $t = 3$ and 0.75 s for VoF and IBM, respectively. The corresponding Reynolds number based on the Taylor length scale (Re_λ) is around 20 for both cases. The values of Kolmogorov, Taylor, and integral length scales at both the stations are

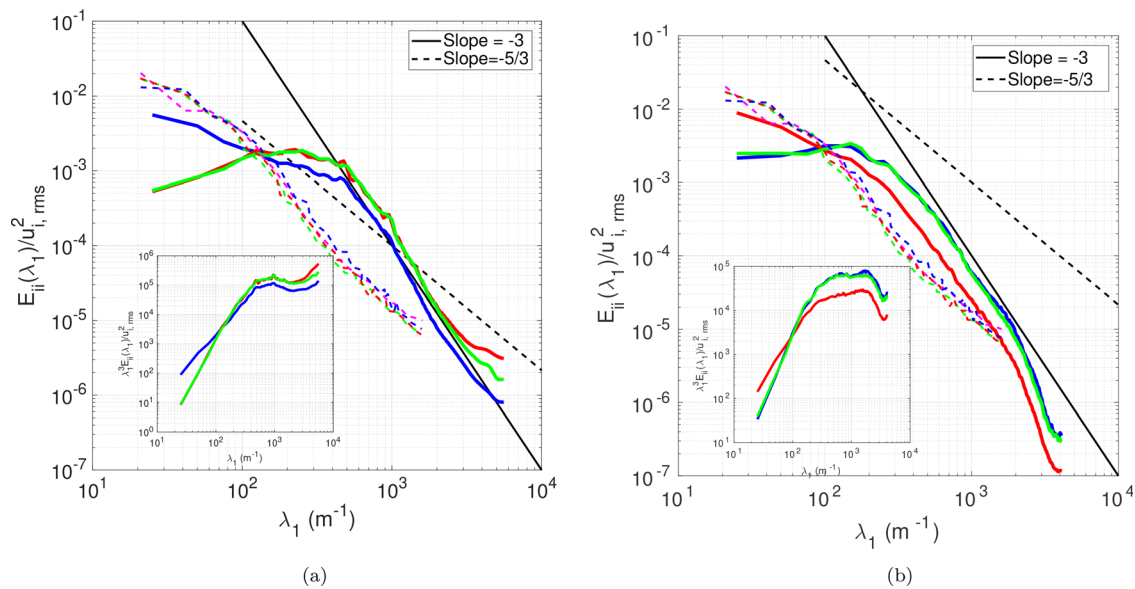


FIG. 4. Spectra of turbulent kinetic energy at the US_{-3} station obtained by (a) VoF and (b) IBM. The velocity fluctuations along the x , y , and z directions are represented in red, blue, and green lines, respectively, where the solid lines are the data from the current simulations and the dashed lines are the data from the literature.

TABLE I. Values of Kolmogorov (η), Taylor (δ), and integral (L) length scale values for BIT at different stations. The values are normalized using the bubble diameter (D).

Simulation	η/D	δ/D	L/D
BIT/VoF: US_{-3}	0.0026	0.0217	0.15
BIT/IBM: US_{-3}	0.0025	0.0441	0.22
BIT/VoF: QS_{-3}	0.0021	0.0211	0.13
BIT/IBM: QS_{-3}	0.002	0.04311	0.21

presented in Table I. It is not surprising that the $-5/3$ slope is completely absent here even at large wavelengths as we do not have a medium to generate shear turbulence in this study. Our results agree well with the previous studies.^{9–11,18} It is also surprising that both VoF and IBM produce similar spectra. Yet, there is one importance difference between Figs. 4(a) and 4(b). In VoF, the kinetic energy along the y -direction seems to be much higher than in the other two directions while the kinetic energy along the x -direction in the IBM simulation seems to be higher than in the other two directions. This difference is attributed to the direction of gravity. We informed in Sec. III that the gravity acts along the y direction in VoF and along the x direction in IBM. It seems that the direction in which the gravity is acting tends to produce more kinetic energy in that direction. This is the reason behind the differences between VoF and IBM in terms of turbulent kinetic energy spectra.

The flow fields corresponding to the energy spectra in Fig. 4 are shown in Fig. 5. The iso-surfaces of a constant Q -criterion are plotted in this figure. We can see from this figure that the flow has just started developing at this time instant in both VoF and IBM simulations. The wakes behind the bubbles are only partially developed. We can also see that the level of intermittency is high at this time instant. Yet, for this time instant, both VoF and IBM show the same trend of -3 slope defined for a wide range of wavelengths. This shows that the bubble

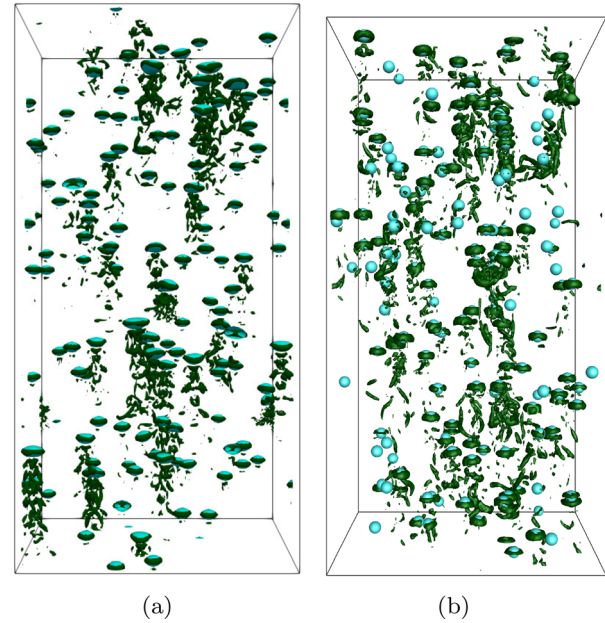


FIG. 5. Visualization of flow structures at the US_{-3} station with Q -criterion ($Q = 5000$) obtained using (a) VoF and (b) IBM.

shape, breakup, and coalescence do not affect the nature of the bubbly energy cascade.

Previous studies reported the spectrum only for the quasi-steady state. The corresponding spectra for the quasi-steady state for our study are shown in Fig. 6. We name this location as QS_{-3} , which stands for quasi-steady location with a -3 energy spectrum slope. Here, the simulation time corresponds to VoF and IBM are 18 and 3.5 s, respectively. The Re_λ values at this location are around 75.

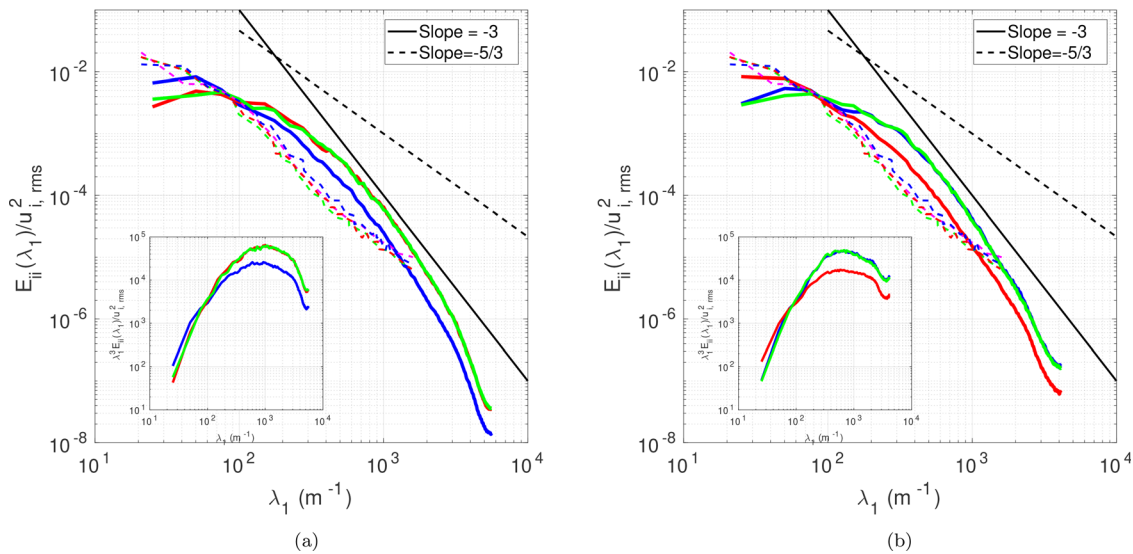


FIG. 6. Spectra of turbulent kinetic energy at the QS_{-3} station obtained using (a) VoF and (b) IBM. The velocity fluctuations along the x , y , and z directions are represented in red, green, and blue lines, respectively, where the solid lines are the data from the current simulations and the dashed lines are the data from the literature.

Classical turbulence theory informs us that as the Re_λ increases, the sink of the turbulent kinetic energy is moved further away from the energy injection point at the spectra, and thus, the wavelength range on which $-5/3$ (here -3 slope) is defined increases. We see a completely different picture when we compare Figs. 4 and 6. The wavelength range on which the -3 slope is defined has become shorter at the QS_{-3} compared with the US_{-3} . At this location also, we do not see any trace of $-5/3$ slope in the spectra as we are dealing with a pure bubble swarm without any influence of shear flows. Here also, we see the impact of the difference in gravity direction in VoF and IBM as the spectrum along the y -direction (blue color line) is distinct in the VoF simulation [Fig. 6(a)] and the spectrum along the x -direction (red color line) is distinct in the IBM simulation [Fig. 6(b)].

The flow field corresponding to the QS_{-3} station is shown in Fig. 7. Here also, iso-surfaces of constant value of Q -criterion are plotted to elucidate the flow field. We note that the number of bubbles in VoF and IBM simulations at this time instant is different. This difference is expected as the bubbles break up and coalesce in VoF while the bubbles in the IBM simulation do not undergo these processes. The wakes behind the bubbles are fully developed, and the intermittent meeting of bubble wakes is largely absent at this time instant despite that the VoF simulation has only a few bubbles. For this kind of flow field, the velocity spectra exhibit a -3 slope.

From this point onward, our study would focus only on the two temporal locations discussed in this subsection: (i) the location where the energy spectrum started to show the best -3 slope, which is in the unsteady state: US_{-3} and (ii) the location that corresponds to quasi-steady state: QS_{-3} . We look at the fine-scale turbulence dynamics at these locations and compare the results with the HIT throughout the rest of the paper.

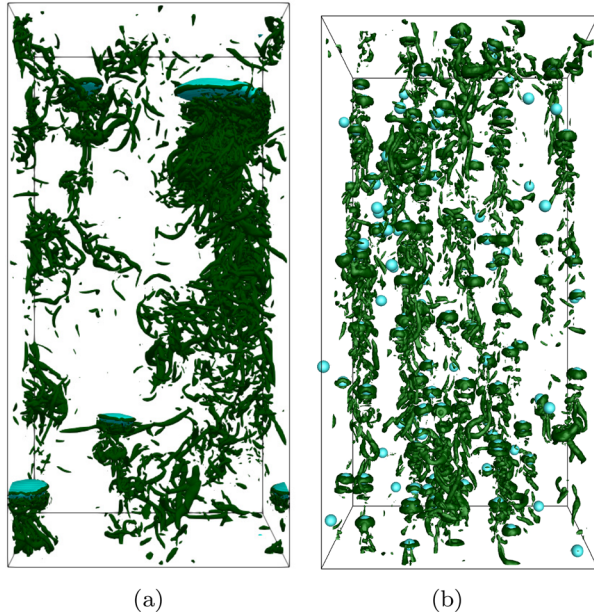


FIG. 7. Visualization of flow structures at the QS_{-3} station with Q -criterion ($Q = 5000$) obtained using (a) VoF and (b) IBM.

B. Mathematical background of the dynamics of fine-scale homogeneous isotropic turbulence

In this paper, we are interested in the velocity gradient tensor (VGT), $A_{ij} = \partial u_i / \partial x_j$. This second-order tensor has the following characteristic equation:

$$\Lambda_i^3 + P\Lambda_i^2 + Q\Lambda_i + R = 0, \quad (2)$$

where Λ_i ($i = 1, 2$, and 3) are the eigenvalues of the velocity gradient tensor, which has three invariants, P , Q , and R , which are given as

$$P = A_{ii}, \quad (3)$$

$$Q = -\frac{1}{2}A_{ij}A_{ji}, \quad (4)$$

$$R = -\frac{1}{3}A_{ij}A_{jk}A_{ki}. \quad (5)$$

The discriminant of Eq. (2) is

$$D = \frac{27}{4}R^2 + Q^3. \quad (6)$$

For an incompressible flow, the trace of the VGT is zero; therefore, $P = 0$. The other two invariants are often used as joint probability density functions to study the topology of the flow. Such studies treat the computational domain as strain- and vorticity-dominating regions, and they seek the presence of flow structures in a statistical sense. Therefore, such studies can fall into the category of studying the kinematics of VGT. In this paper, we are interested in the dynamics of the VGT where we follow the fluid element, which consists of vorticity and strain and study what happens to the VGT characteristics of this fluid element as we follow it. To this end, we need to derive and analyze the governing equations of the VGT and its non-zero invariants. This section briefly discusses how these equations are derived and used for the dynamical analysis of VGT.

1. Governing equations

The dynamical equation of VGT is obtained from the following Navier–Stokes equations:

$$\frac{\partial u_i}{\partial t} + u_k \frac{\partial u_i}{\partial x_k} = -\frac{\partial p}{\partial x_i} + \nu \frac{\partial^2 u_i}{\partial x_k \partial x_k}. \quad (7)$$

Differentiating the above equation with respect to x_j leads to^{35,36}

$$\frac{\partial A_{ij}}{\partial t} + u_k \frac{\partial A_{ij}}{\partial x_k} + A_{ik}A_{kj} = -\frac{\partial^2 p}{\partial x_i \partial x_j} + \nu \frac{\partial^2 A_{ij}}{\partial x_k \partial x_k}. \quad (8)$$

Denoting the pressure and viscous Hessian matrices as $H_{ij}^p = \frac{\partial^2 p}{\partial x_i \partial x_j}$ and $H_{ij}^v = \nu \frac{\partial^2 A_{ij}}{\partial x_k \partial x_k}$, the above equation can be written as^{35,36}

$$\frac{DA_{ij}}{Dt} + A_{ik}A_{kj} = -H_{ij}^p + H_{ij}^v, \quad (9)$$

where $\frac{D}{Dt}$ is the total derivative term given as $\frac{D}{Dt} = \frac{\partial}{\partial t} + u_k \frac{\partial}{\partial x_k}$.

Although Eq. (9) is a useful equation, it can be further improved by segregating the effects of dilatational and deviatoric parts of the pressure Hessian as^{35,36}

$$H_{ij}^P = H_{ij}^{P*} + H_{ij}^{P'}, \quad (10)$$

where H_{ij}^{P*} and $H_{ij}^{P'}$ are the dilatational and deviatoric parts of the pressure Hessian matrix and they are given as

$$H_{ij}^{P*} = H_{kk}^P \frac{\delta_{ij}}{3}, \quad (11)$$

$$H_{ij}^{P'} = H_{ij}^P - H_{kk}^P \frac{\delta_{ij}}{3}. \quad (12)$$

Substituting Eq. (10) in Eq. (9),

$$\frac{DA_{ij}}{Dt} + A_{ik}A_{kj} = -H_{kk}^P \frac{\delta_{ij}}{3} - H_{ij}^{P'} + H_{ij}^V. \quad (13)$$

Since the dilatational part of the pressure Hessian is local, it does not act as a source term. Therefore, this term can be brought to the left-hand side as^{35,36}

$$\frac{DA_{ij}}{Dt} + A_{ik}A_{kj} + H_{kk}^P \frac{\delta_{ij}}{3} = -H_{ij}^{P'} + H_{ij}^V. \quad (14)$$

We can now write the dilatational part of the pressure Hessian in terms of the local velocity gradients as follows. Note that the trace of the A_{ij} is zero due to incompressibility, setting $i = j$ in Eq. (14), we get the equation for the dilatational part of the pressure Hessian as

$$A_{ik}A_{ki} = -H_{ii}^{P'}. \quad (15)$$

Substituting Eq. (15) in Eq. (13),

$$\frac{DA_{ij}}{Dt} + A_{ik}A_{kj} - A_{ik}A_{ki} \frac{\delta_{ij}}{3} = -H_{ij}^{P'} + H_{ij}^V. \quad (16)$$

Grouping together the source terms as $H_{ij} = -H_{ij}^{P'} + H_{ij}^V$, the governing equation of VGT in final form is^{35,36}

$$\frac{DA_{ij}}{Dt} + A_{ik}A_{kj} - A_{ik}A_{ki} \frac{\delta_{ij}}{3} = H_{ij}, \quad (17)$$

where $H_{ij} = -H_{ij}^{P'} + H_{ij}^V$ and $H_{ij}^{P'}$ is the deviatoric part of the pressure Hessian and H_{ij}^V is the viscous term.

From Eq. (17), we can also deduce the governing equations of Q and R . First, we need to derive the governing equation for the double and triple products and then taking the trace of the results would yield the following governing equations for Q and R :^{35,36}

$$\frac{DQ}{Dt} = -3R - A_{ij}H_{ji}, \quad (18)$$

$$\frac{DR}{Dt} = \frac{2}{3}Q^2 - A_{ij}A_{jk}H_{ki}. \quad (19)$$

If we neglect all the source terms by setting $H_{ij} = 0$, then we obtain the restricted Euler equations as^{35,36}

$$\frac{DQ}{Dt} = -3R, \quad (20)$$

$$\frac{DR}{Dt} = \frac{2}{3}Q^2. \quad (21)$$

As seen from the above equations, the dynamical equations of the VGT invariants are functions of the invariants themselves when the source terms are neglected.

2. Conditional mean trajectories (CMT)

The best way to obtain VGT dynamics is to calculate the terms in Eqs. (17)–(19) by following a fluid particle. This technique, however, is cumbersome on many levels. First, particle tracking must be carried out concurrently along with the simulation. Second, we need to invoke sophisticated mathematical concepts to accurately track particle displacement and its integration. Finally, we must track a large number of fluid particles to reach statistical convergence. To circumvent these difficulties, a new conditional averaging method was proposed by Martin *et al.*³⁵ In this method, the mean time derivative of the invariants is conditioned on the invariants themselves. As such, the mean time derivatives of the VGT invariants are functions of the invariants and they are plotted in the phase space map of the invariants. Therefore, we compute the mean time derivative of invariants at all the points in the phase space of Q and R using the conditional averaging technique as shown below:

$$\dot{Q}(Q, R) = \left\langle \frac{DQ}{Dt} \right\rangle_{R,Q} = -3R - \langle A_{ij}H_{ji} |_{R,Q} \rangle, \quad (22)$$

$$\dot{R}(Q, R) = \left\langle \frac{DR}{Dt} \right\rangle_{R,Q} = \frac{2}{3}Q^2 - \langle A_{ij}A_{jk}H_{ki} |_{R,Q} \rangle. \quad (23)$$

We use 20 snapshots around each of US_{-3} and QS_{-3} stations to compute the above equations. The above two equations form the components of a vector, and when this vector quantity is plotted in the (Q, R) phase space, the resulting streamlines are called conditional mean trajectories (CMTs).

Note that Eqs. (22) and (23) consist of dynamics belonging to the inertia, pressure and viscosity. We can consider the effects of these individually as follows. For instance, the CMTs for the inertial system are obtained using the following equations:

$$\dot{Q}_{RE}(Q, R) = \left\langle \frac{DQ_{RE}}{Dt} \right\rangle_{R,Q} = -3R, \quad (24)$$

$$\dot{R}_{RE}(Q, R) = \left\langle \frac{DR_{RE}}{Dt} \right\rangle_{R,Q} = \frac{2}{3}Q^2. \quad (25)$$

Similarly, the CMT for the VGT system which is subject to pressure forces alone can be obtained as

$$\dot{Q}_P(Q, R) = \left\langle \frac{DQ_P}{Dt} \right\rangle_{R,Q} = \langle A_{ij}H_{ji}^{P'} |_{R,Q} \rangle, \quad (26)$$

$$\dot{R}_P(Q, R) = \left\langle \frac{DR_P}{Dt} \right\rangle_{R,Q} = \langle A_{ij}A_{jk}H_{ki}^{P'} |_{R,Q} \rangle, \quad (27)$$

where $H_{ij}^{P'}$ is given in Eq. (12).

Finally, the equations for the VGT dynamical system subject to only viscous effects can be written as

$$\dot{Q}_V(Q, R) = \left\langle \frac{DQ_V}{Dt} \right\rangle_{R,Q} = -\langle A_{ij}H_{ji}^V |_{R,Q} \rangle, \quad (28)$$

$$\dot{R}_V(Q, R) = \left\langle \frac{DR_V}{Dt} \right\rangle_{R,Q} = -\langle A_{ij}A_{jk}H_{ki}^V |_{R,Q} \rangle. \quad (29)$$

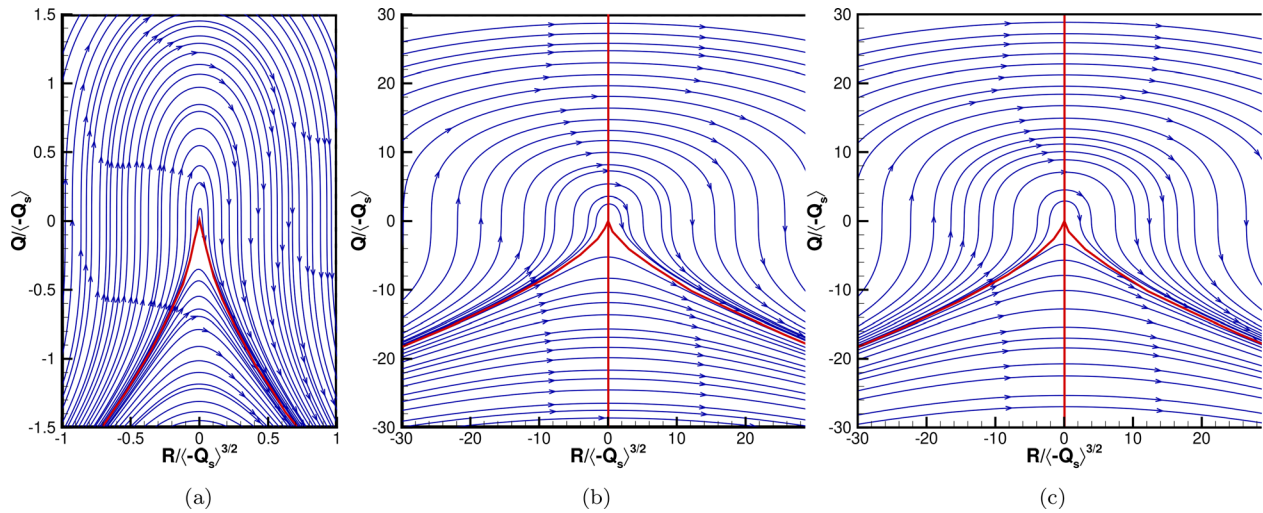


FIG. 8. CMT of VGT inertial dynamics obtained for (a) HIT, (b) VoF, and (c) IBM. The BIT sub-figures are plotted for the US_{-3} station.

Equations (22)–(29) are important for our study as we compute these conditionally averaged quantities and plot them as CMTs in Q, R phase space.

As mentioned before, both \dot{Q} and \dot{R} form two components of a vector. Thus, we can also compute the magnitude of each of these vectors as

$$M(\dot{Q}, \dot{R}) = \left\langle \sqrt{\left(\frac{\dot{Q}}{\langle -Q_s \rangle^2} \right)^2 + \left(\frac{\dot{R}}{\langle -Q_s \rangle^2} \right)^2} \right\rangle, \quad (30)$$

where $Q_s = -\frac{1}{2}s_{ij}s_{ij}$ with s_{ij} is the strain-rate tensor.

$$M(\dot{Q}_{RE}, \dot{R}_{RE}) = \left\langle \sqrt{\left(\frac{\dot{Q}_{RE}}{\langle -Q_s \rangle^2} \right)^2 + \left(\frac{\dot{R}_{RE}}{\langle -Q_s \rangle^2} \right)^2} \right\rangle, \quad (31)$$

$$M(\dot{Q}_P, \dot{R}_P) = \left\langle \sqrt{\left(\frac{\dot{Q}_P}{\langle -Q_s \rangle^2} \right)^2 + \left(\frac{\dot{R}_P}{\langle -Q_s \rangle^2} \right)^2} \right\rangle, \quad (32)$$

$$M(\dot{Q}_V, \dot{R}_V) = \left\langle \sqrt{\left(\frac{\dot{Q}_V}{\langle -Q_s \rangle^2} \right)^2 + \left(\frac{\dot{R}_V}{\langle -Q_s \rangle^2} \right)^2} \right\rangle. \quad (33)$$

In Secs. IV C–IV F, we present the dynamics of inertial, pressure, viscous, and overall terms along with their magnitudes to elucidate the role of breakup and coalescence and to reveal the differences of bubbly VGT dynamics with that of the HIT.

C. Inertial dynamics

1. Homogeneous isotropic turbulence

We first present the inertial dynamics of the classical HIT case as a detailed explanation of fine-scale HIT dynamics is still lacking in the literature. The conditional mean trajectories of the inertial system for the case of HIT are depicted in Fig. 8(a). We can see from this figure that the CMTs are attracted toward the right branch of the curve

$D = 0$. This is the typical behavior of the inertial system, and this was first observed by Vieillefosse⁴⁵ and later various studies have confirmed such a pattern.^{36,37,46,47}

In terms of flow physics, Fig. 8(a) can be explained using a simple example as shown in Fig. 9. Let us consider a fluid element, which has non-zero strain components of s_{11} , s_{22} , and s_{33} . As we know, this element also has vorticity in it and let us say that the predominant component here is ω_1 , that is the fluid element rotates about the axis “1.” Now, let us consider that this fluid element has more vortex stretching than the strain self-amplification. This means that the value of R is negative [recall that $R = -\frac{1}{3}(s_{ij}s_{jk}s_{ki} + \frac{3}{4}\omega_i s_{ij} \omega_j)$]. Such a configuration is possible for our simple case when s_{11} is positive while s_{22} and s_{33} are negative. For example, let us say $s_{11} = 1$, $s_{22} = -0.5$, and $s_{33} = -0.5$. Since these components form the diagonal of the strain-rate tensor, the sum of these components must be zero (i.e., $s_{11} + s_{22} + s_{33} = 0$). For this case, the strain self-amplification value will be less than the value of vortex stretching. Particularly, for this case, the strain self-amplification is negative (i.e., $-s_{ij}s_{jk}s_{ki} < 0$).

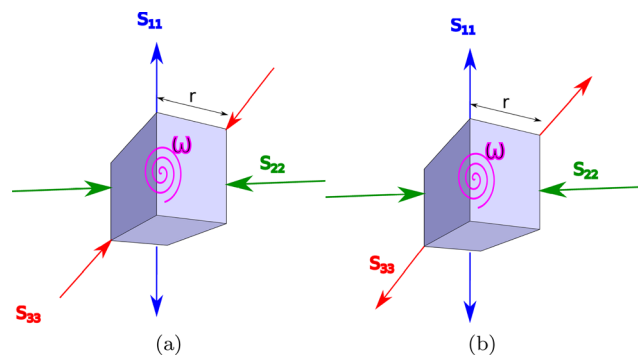


FIG. 9. A typical fluid element with strain and vorticity where (a) enstrophy production is greater than strain production and (b) strain production is greater than enstrophy production.

We know that strain and vorticity are governed by the following equations:

$$\frac{D}{Dt} \frac{1}{2} \omega_i \omega_i = \omega_i s_{ij} \omega_j + \nu \omega_i \frac{\partial^2 \omega_i}{\partial x_j \partial x_j}, \quad (34)$$

$$\frac{D}{Dt} \frac{1}{2} s_{ij} s_{ij} = -s_{ij} s_{jk} s_{ki} - \frac{1}{4} \omega_i s_{ij} \omega_j - s_{ij} \frac{\partial p}{\partial x_i \partial x_j} + \nu s_{ij} \frac{\partial^2 s_{ij}}{\partial x_j \partial x_j}. \quad (35)$$

From these equations, we see that the source term for strain is strain self-amplification and the source term of vorticity is vortex stretching. We also see that vortex stretching also acts as a sink term for strain.

From the above equations, it is easy to see that the total time derivative of vorticity and strain are positive and negative as $\omega_i s_{ij} \omega_j$ is positive and $-s_{ij} s_{jk} s_{ki}$ is negative for our simple case when $R < 0$. This means that, as the fluid element evolves, its vorticity would increase and its strain would decrease. The increase in vorticity due to stretching is well documented, and it can be easily explained for this illustrative example too.⁴⁸ Since there are two compressing and one extensive strain for $R < 0$, we see that the fluid element in Fig. 9(a) would be stretched along the direction “1” and the value of “r” [see Fig. 9(a)] would shrink. As the moment of inertia of this fluid element is proportional to “r,” a decrease in it would decrease the fluid element’s moment of inertia. As a result, to conserve angular momentum, the angular velocity of the fluid element (i.e., vorticity) increases.

At this point, one might tend to think that the vorticity would continue to increase toward infinity for this case. In reality, however, stronger vortex stretching would lead to reduced strain. This can be seen from the fact that the positive value of $\omega_i s_{ij} \omega_j$ for this simple case is leading to a negative value of $-s_{ij} s_{jk} s_{ki}$. Moreover, we also observe in Eq. (35) that the vortex stretching term acts as a sink term for strain. Once the strain decreases, it would weaken vortex stretching as enstrophy production occurs due to a complex interaction of strain and vorticity. Due to this, the growth of vorticity for this simple case is bounded. Therefore, although the vorticity starts increasing as the fluid element evolves in time, the rate of its increase becomes weaker and weaker as the element continues to evolve. For this simple case, there are two possibilities concerning the initial state of strain and vorticity: (i) vorticity dominating strain and (ii) strain dominating vorticity.

Let us consider the first possibility. Let us say that the same fluid element has more vorticity than strain initially. This fluid element would fall in the upper-left quadrant of the (Q, R) phase space. As we saw earlier, once this element starts evolving, its vorticity would increase with a continually reduced rate of increase and its strain would decrease. Therefore, the fluid element would start moving upward in the $(+Q, -R)$ quadrant of the (Q, R) phase space. At the same time, the production of vorticity would decrease because of the weakened strain and the production of strain would decrease because of the negative $-s_{ij} s_{jk} s_{ki}$. Due to this, the balance between these two production terms would remain very small. This is the reason why we see the fluid element is moving along a near-straight-line in the $(+Q, -R)$ quadrant of the (Q, R) phase space.

As the strain continues to decrease during the evolution of the fluid element, there comes a point during the evolution of the fluid element where there is so much vorticity but not enough strain to stretch the element. At this point, there is little vortex stretching, which causes a little decrease in strain. Therefore, from this point onward, the fluid element evolves with the balance between the production terms of

strain and vorticity approaching zero from the negative value. Once enough strain has been generated, the fluid element now finds itself in the positive R side of the (Q, R) phase space with the state depicted in Fig. 9(b) where we have two extensive strains and one compressive strain.

In the new configuration shown in Fig. 9(b), the strain self-amplification value would be positive (i.e., $-s_{ij} s_{jk} s_{ki} > 0$), which leads to an increase in the strain as the fluid element evolves in the upper-right quadrant of the (Q, R) phase space. At the same time, the value of “r” would increase due to stretching along the direction “3.” This would lead to an increase in moment of inertia, and thus, the vorticity would start decreasing. Now we have a situation where the strain would continually increase without any bound, and the vorticity would continually decrease without any bound too. Since the positive quadrant of the (Q, R) phase space has more vorticity than strain, there will be enstrophy production albeit it has a negative value. Due to this, the difference between the production terms of strain and vorticity would be small yet increasing as the fluid element evolves in the $(+Q, +R)$ quadrant of the (Q, R) phase space. This is the reason why we see another near-straight-line behavior in this quadrant.

As the fluid element continues to evolve, there comes a point where the amount of strain would exceed the amount of vorticity. This would take the fluid element to the lower-right quadrant of the (Q, R) phase space. Once the fluid element entered into this quadrant, the enstrophy production term would become negligible as the amount of vorticity is too small. Therefore, the R term is now entirely controlled by the strain self-amplification due to which the R value continually increases along the positive horizontal axis. Moreover, here the strain also increases without bound. As a result, the value of strain and its production evolves toward infinity. Thus, the fluid element evolves toward finite-time divergence along the right-hand branch of the equation $D = 0$ in the $(-Q, R)$ quadrant of the (Q, R) phase space.

In the second possibility of the simple case that we consider, there is more strain compared to vorticity at the initial time. We know that for our simple case when $R < 0$, the strain would go down and the vorticity would go up with the rate of increase continually decreasing. As a result, the fluid element would go up in the $(-Q, -R)$ quadrant of the (Q, R) phase space. If the amount of vorticity is reasonable enough, this element would eventually evolve to the upper-left quadrant of the (Q, R) phase space and all the mechanisms that we explained in this section would occur for this element as it reaches the finite-time divergence. In general, the fluid element that lies above the left branch of the $D = 0$ equation would undergo such an evolution. The fluid element that lies under the left-branch of $D = 0$ equation, however, has little vorticity, and as such even before the enstrophy production starts kicking in, the strain dominance slowly brings this element to the right-hand side of the R axis where the fluid element now takes the state of the one shown in Fig. 9(b), which helps the fluid element to generate more strain while the vorticity is continually decreased. As the amount of vorticity is already too low for this element, the R term is now entirely controlled by the strain self-amplification, which takes the fluid element further right in the $(-Q, R)$ quadrant of the (Q, R) phase space toward the right-hand branch of $D = 0$ equation. Thus, for this second possibility also, the fluid element evolves to a finite-time divergence marked with unrestricted growth of strain and its production. This is the first time a detailed explanation of the movement of the fluid element within the (Q, R) phase space under the inertial dynamics is presented in the literature for HIT.

TABLE II. Values of $M(\dot{Q}_{RE}, \dot{R}_{RE})$ for BIT and HIT.

Simulation	$M(\dot{Q}_{RE}, \dot{R}_{RE})$
HIT	1.9
BIT/VoF: US_{-3}	25.7
BIT/IBM: US_{-3}	24.8
BIT/VoF: QS_{-3}	18.3
BIT/IBM: QS_{-3}	19.2

Having looked at the mechanisms of fluid element evolution in the (Q, R) phase space, let us now look at some quantitative results. The magnitude of the Euler terms [i.e., $M(\dot{Q}_{RE}, \dot{R}_{RE})$] for HIT is given in the first row of Table II. This value agrees well with the literature,^{36,37,46,47} which in turn gives us the confidence that the conditional averaging tool has indeed been developed in line with the literature standards.

2. Bubble induced turbulence

Having established the behavior of inertial terms for HIT, let us now focus on the bubbly flows. Figures 8(b) and 8(c) represent the CMTs of inertial terms at the US_{-3} station obtained using VoF and IBM, respectively. These figures appear qualitatively similar to that of HIT. As a result, the dynamics of inertial terms in VGT appear to be that of the HIT. Yet, the magnitude of these quantities, as given in Table II, is much larger in BIT than in the HIT. One plausible explanation for this large magnitude of inertial terms lies in the fact that at this time instant, the vortex shedding has just started and this generally gives rise to stronger vorticity while the rest of the domain is occupied with strain. Another important result we obtain from Fig. 8 is that the bubble topology, breakup and coalescence do not play any role in setting the inertial dynamics at the small scales. This result is highly valuable for modeling small scale turbulence.

Finally, Fig. 10 presents the inertial dynamics of VGT at the QS_{-3} station where the bubble breakup and coalescence is nominal. Figures 8 and 10 are identical, and we conclude that the dynamics of

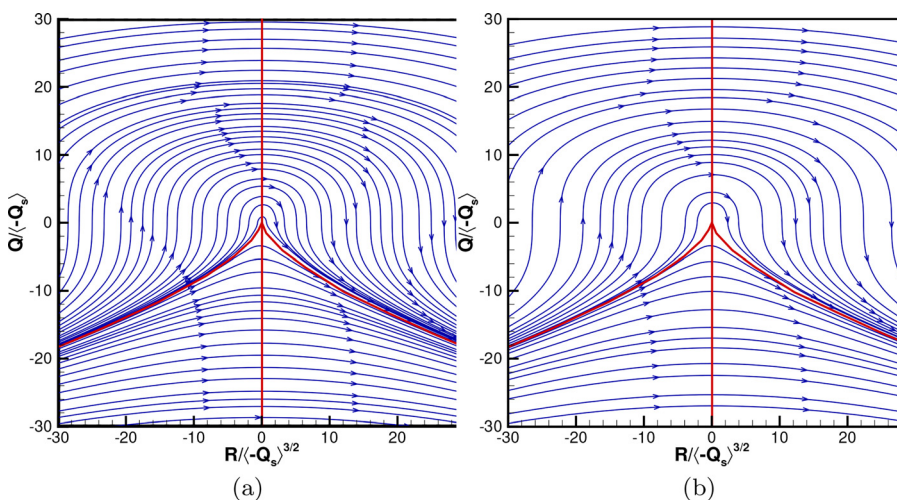
the fluid element when it is subject to no sources remain the same in HIT as well as BIT and the bubble topology and deformation do not influence the inertial dynamics. The only difference between HIT and BIT regarding the inertial dynamics is once again noted in the magnitudes of the inertial terms as reported in Table II. Since the bubble wakes have fully met at the QS_{-3} station, we tend to expect the intensity of velocity gradients to reduce. This we notice in Table II, yet in comparison with the HIT, the magnitude of inertial terms is still larger. This makes us conclude that the BIT produces stronger velocity gradients. One plausible explanation for this strong velocity gradients in BIT is the disruptive presence of the bubbles that, in some sense, break the uniformity of the flow and, thus, cause steep velocity gradients.

D. Pressure dynamics

1. Homogeneous isotropic turbulence

Having discussed the dynamics of the inertial term, this section explains what happens to the time evolution of a fluid element when it is subject to pressure effects. First, let us consider the case of HIT whose CMTs for pressure dynamics are presented in Fig. 11(a). The vector lines are almost parallel to each other moving from right to left. We also note the finite-time divergence in the pressure dynamics as the vector lines in Fig. 11(a) continues to the left indefinitely. It is generally believed that the pressure dynamics act as an opposing force against the inertial dynamics.³⁵ Evidence can be seen from Figs. 8(a) and 11(a) that the vector lines of inertial and pressure dynamics oppose each other. We discuss the pressure dynamics for two initial conditions for fluid elements using the same simplified case presented in Fig. 9 below.

As we observed earlier, the strain and its production continue to increase for a fluid element in the $(-Q, +R)$ phase space when there is no source. This is because of two stretching directions as shown in Fig. 9(b), which lead to more strain and reduction in vorticity. If we consider the same fluid element in the same quadrant but are now subject to a pressure source, the pressure dynamics act in such a way that the preference for producing more strain for a strain-dominated fluid element diminishes as the fluid element evolves in time. Due to this, at some point in time, the fluid element evolves to the negative R


FIG. 10. CMT of VGT inertial dynamics obtained for (a) VoF and (b) IBM at the QS_{-3} station.

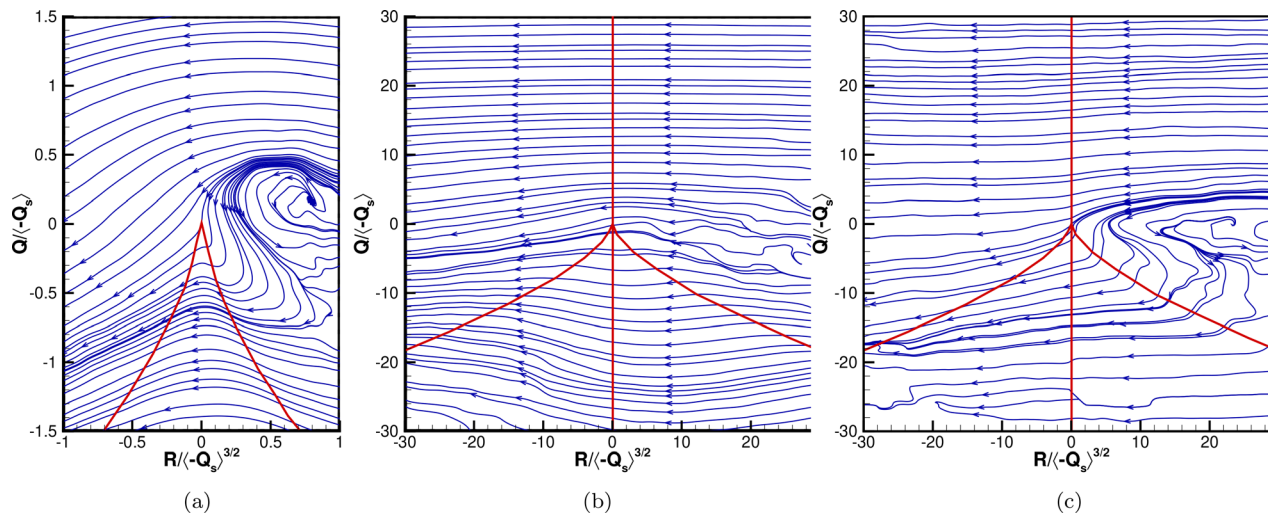


FIG. 11. CMT of VGT pressure dynamics obtained for (a) HIT, (b) VoF, and (c) IBM. The BIT sub-figures are plotted for the US_{-3} station.

side of the (Q, R) phase space. One might wonder how does the fluid element stay strain-dominated while the tendency to produce strain progressively diminished during its evolution. We need to understand that, while opposing the inertial dynamics, the predominant nature of the pressure Hessian is to generate deformations in the fluid element, which in turn increases the strain.^{49,50} Consequently, the tendency to create strain diminishes and the enstrophy production becomes dominant at some point during the evolution. The difference between magnitudes of strain and vorticity remains almost constant as the pressure Hessian produces strain while the fluid element also moves toward the state where it tends to generate more enstrophy. Therefore, the fluid element never moves downward in the (Q, R) phase space. Thus, this element also moves toward to state where the magnitude of velocity gradients become infinity.

Second, we consider a fluid element in the top-right quadrant [i.e., $(+Q, +R)$ quadrant] of the (Q, R) phase space. As we saw earlier, when there is no source, this fluid element tends to move down in the (Q, R) phase space as it has more tendency to generate strain and to reduce vorticity and due to this the strain magnitude increases making the sign of the second invariant of VGT to change from positive to negative. At the same time, we have just found out that the role of pressure dynamics is to restrict the strain self-amplification mechanism that produces strain. As a result, the fluid element in this quadrant when subject to pressure source does not move down in the (Q, R) phase space. Rather, it moves to the left as the pressure Hessian dampens the strain production mechanism making the third invariant of the VGT change sign from positive to negative during the evolution. During this, the magnitude of vorticity tends to increase as its production increases, but, at the same time, the pressure Hessian deforms the fluid element causing more strain. As such, the difference between the strain and vorticity magnitudes remains the same during the evolution. Here also, the magnitude of velocity gradients continue to increase and approach infinity as the fluid element evolves. These are the mechanisms that Fig. 11(a) reveals through the vector lines.

The magnitude of pressure Hessian for HIT is given in the first row of Table III. The magnitude of pressure dynamics is almost close

to that of inertial dynamics reminding us once again that they both act against one another. The value in Table III is also consistent with the literature.^{36,37,46,47}

2. Bubble induced turbulence

Now, let us focus on BIT. Our goal here is twofold. Figures 11(b) and 11(c) show the pressure dynamics for the BIT obtained using VoF and IBM, respectively, for the US_{-3} station. Comparing with Fig. 11(a), we see that the pressure dynamics of BIT look similar to that of the HIT. Here also, the vector lines move from right to left in all the quadrants of the (Q, R) phase space. Thus, the explanations rendered before in this section are also applicable to BIT. Comparing Figs. 11(b) and 11(c), we also learn that the pressure dynamics are independent of breakup and coalescence as these two figures look relatively similar. Looking at the magnitudes of the pressure dynamics for BIT in Table III (the second and third rows), we see some intriguing differences concerning HIT. The magnitude of pressure dynamics in BIT is way larger than in HIT. These values are similar to values reported in the near-field of turbulence generated by a fractal grid.³⁸ For them, the location where they report very high values of pressure Hessian dynamics is highly intermittent as the wakes from the turbulence-generating grids start interacting with each other. Our station US_{-3} is also marked by highly intermittent turbulence as the wakes behind the bubbles have just started developing and start meeting intermittently

TABLE III. Values of $M(\dot{Q}_P, \dot{R}_P)$ for BIT and HIT.

Simulation	$M(\dot{Q}_P, \dot{R}_P)$
HIT	2.1
BIT/VoF: US_{-3}	105.6
BIT/IBM: US_{-3}	100.5
BIT/VoF: QS_{-3}	20.5
BIT/IBM: QS_{-3}	21.1

with one other. Therefore, it seems the intermittent nature of turbulence with intense vortices leads to very high magnitudes of pressure Hessian both in BIT and in the near-field of turbulence generated by a fractal grid.

In the case of turbulence generated by a fractal grid, although the magnitude of pressure Hessian dynamics was strong in the near-field, the magnitude values become similar to that of HIT in the downstream.³⁸ We see from Table III (see the last two rows of this table), however, in BIT that the pressure Hessian magnitude never becomes similar to that of HIT as the values for the station QS_{-3} also much larger than that of HIT albeit that the values have decreased drastically from US_{-3} to QS_{-3} stations. This shows that the dominance of pressure Hessian is not simply due to intermittency but rather it appears to be a feature related to strain-dominated flows. (Please refer to Paper II on the kinematic aspect of strain dominance in BIT.⁶⁷) We also learn from Fig. 12 that the pressure dynamics remain the same as the bubbles evolve irrespective of whether they undergo any deformation, even in the QS_{-3} station.

E. Viscous dynamics

1. Homogeneous isotropic turbulence

We have seen in Secs. IV C and IV D that the magnitude of VGT tends to diverge in finite time. We might wonder if they ever get reduced. This section presents the mechanism by which the magnitudes of VGT are reduced and eventually destroyed, and the mechanism is viscous dissipation. This section deals with the viscous dynamics of a fluid element, and we compare the results of BIT and HIT along with studying the effects of breakup and coalescence in setting up the viscous dynamics.

Figure 13(a) shows the dynamics of a fluid element when it is subject to viscous effects for HIT. The story that Fig. 13(a) reveals is very simple and intuitive. Irrespective of which quadrant the fluid element is initially, it moves toward the origin of the (Q, R) phase space as the element starts evolving in time. This is due to the action of viscosity, which acts on the fluid element to dissipate the turbulent kinetic energy and, thus, the velocity gradient magnitudes. We also see

that most of the vector lines lie inside their quadrants. In terms of flow physics, this paints the following picture.

Let us consider a fluid element with more enstrophy than strain and more tendency to generate strain over the tendency to generate vorticity [see Fig. 9(b)]. The moment this fluid element is subject to viscosity; the viscosity will try to destroy all of its velocity gradients. To that end, it will first stop the dominance of strain production and, thus, reduce the magnitude of strain. Since the enstrophy production of this element is negative and the vorticity is decreasing with the evolution, the effect of viscosity on vorticity is minimum. Yet, the action of viscosity on the enstrophy production is also to destroy it and, thus, to reduce the magnitude of vorticity in that fluid element. Thus, if the strain production is reduced by half during the evolution of the fluid element by viscosity, then the enstrophy production is also reduced by half. Consequently, the amount of strain and vorticity is also reduced by half as the fluid element evolves. The result is that the element will continue to stay vorticity-dominated with a preference to generate more strain, but the magnitudes of these processes continually decrease as the element evolves. Thus, the positive value of the second VGT invariant remains positive but the value keeps coming down as the element evolves. Similarly, the positive sign of the third VGT invariant also remains positive but its magnitude keeps getting reduced. The action of viscosity is complete when all the magnitudes of the VGT are brought to nought. Thus, the values of the second and third invariants of VGT eventually reduce to zero. Due to this, the fluid element remains in the same quadrant of the (Q, R) phase space throughout its evolution. This explanation is applicable for any fluid elements irrespective of which quadrant of the (Q, R) phase space they found themselves in.

The magnitude of the viscous dynamic term is shown in the first row of Table IV. Compared with the inertial and pressure dynamics, the viscous dynamics are weak in terms of their magnitude and the value of the magnitude agrees well with the literature.^{36,37,46,47}

2. Bubble induced turbulence

Let us now look at the effect of breakup and coalescence on the viscosity VGT dynamics of BIT. Figures 13(b) and 13(c) present the

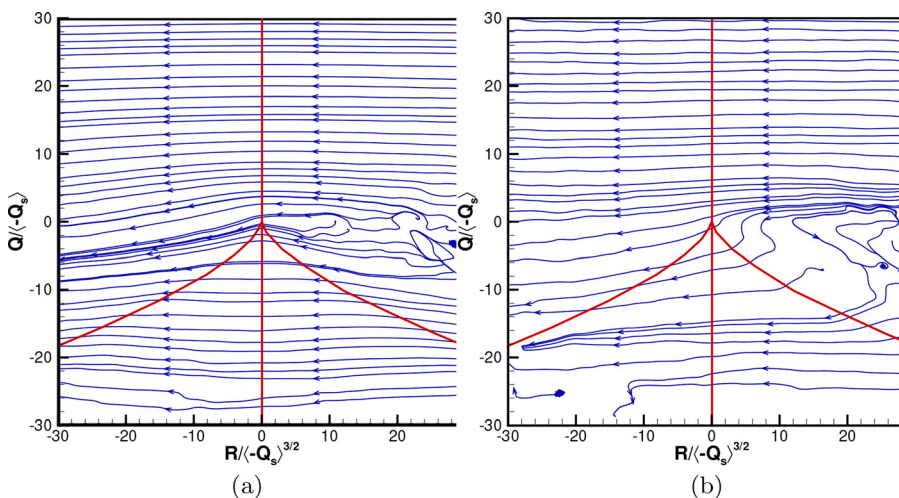


FIG. 12. CMT of VGT pressure dynamics obtained for (a) VoF and (b) IBM at the QS_{-3} station.

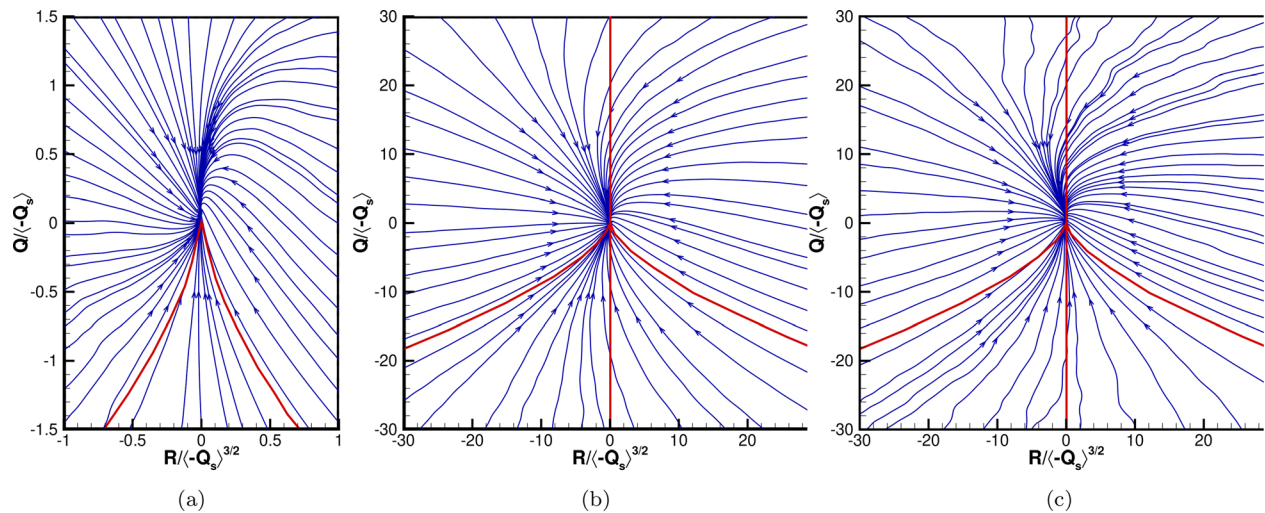


FIG. 13. CMT of VGT viscous dynamics obtained for (a) HIT, (b) VoF, and (c) IBM. The BIT sub-figures are plotted for the US_{-3} station.

VGT dynamics of a fluid element subject to viscosity when the bubbles undergo deformation and when bubbles do not undergo deformation, respectively, at the US_{-3} station. The first observation from these figures is that the viscosity VGT dynamics of BIT appears to be similar to that of the HIT as Figs. 13(b) and 13(c) also contain vector lines that move toward the origin of the (Q, R) phase space and the most of the vector lines seem to be in the same quadrant as the fluid element evolves in time. Therefore, the physics of viscosity VGT dynamics of HIT discussed before can easily be extended to the BIT. The only difference of bubbly VGT viscous dynamics to HIT appears in terms of the magnitudes of the viscosity dynamics terms. Table IV presents the values of magnitudes of viscosity VGT dynamics for BIT in the second and third rows of the table. As with the inertial and pressure dynamics, the magnitudes of the viscosity dynamics also are quite large compared with the HIT. Once again, this could be attributed to the fact that both strain and vorticity are stronger at the QS_{-3} station and, thus, stronger viscosity dynamics are required to smooth out these. Figures 13(b) and 13(c) also make it clear that, once again, the bubble topology, breakup, and coalescence play no role in determining the fine-scale dynamics of BIT as we do not see any difference between these figures.

Finally, Fig. 14 presents the VGT dynamics of bubbly flows when it is subject to viscosity at the QS_{-3} station. At this station also, the viscosity VGT dynamics of BIT appears to be the same as that of HIT with bubble deformation does not influence the viscosity VGT dynamics [compare Figs. 14(a) and 14(b)]. Since the magnitude of velocity

gradients has reduced at this station, the magnitude of viscosity VGT dynamics has come down at this station (see the last two rows of Table IV). Yet, the magnitudes are still much larger than the HIT. These values also reveal that there is no influence of bubble breakup and coalescence on the viscosity VGT dynamics.

F. Overall dynamics

1. Homogeneous isotropic turbulence

So far we have been looking at the VGT dynamics of a fluid element when it is subject to no source and when it is subject to pressure and viscous sources. To recall from the main results from Secs. IV C–IV E, we know that the fluid element tends to evolve toward the state of more strain over vorticity and more strain production over enstrophy production when there is no source. We also found that the action of pressure dynamics is mainly to oppose the strain production while the pressure Hessian itself causes strain to generate. Finally, the action of viscosity is to reduce the magnitude of the VGT dynamics and eventually destroy them. This section presents results as to what happens when all these effects are included as we track the fluid element.

Figure 15(a) presents the overall VGT dynamics of HIT. The figure looks similar to the one reported in the literature.^{36,37,46,47} Here, the CMTs move cyclically toward the origin. Each shape of the CMTs for every cycle resembles the shape of the joint probability density between the second and third invariants of the VGT.

In terms of flow physics, the CMTs offer us the following explanation. Let us consider a fluid element having more strain over vorticity and more enstrophy production over strain production. When there are no sources, this element would tend to evolve toward a state where the strain production and strain increase indefinitely (i.e., toward the right branch of $D = 0$ curve) as we noted earlier. The action of pressure Hessian, however, averts such behavior as the pressure dynamics act against the strain production. Thus, the pressure dynamics act as a constraint against strain increasing indefinitely. At the same time, the viscous dynamics tend to pull the fluid element toward

TABLE IV. Values of $M(\dot{Q}_V, \dot{R}_V)$ for BIT and HIT.

Simulation	$M(\dot{Q}_V, \dot{R}_V)$
HIT	0.2
BIT/VoF: US_{-3}	6.5
BIT/IBM: US_{-3}	6.3
BIT/VoF: QS_{-3}	6.3
BIT/IBM: QS_{-3}	6.3

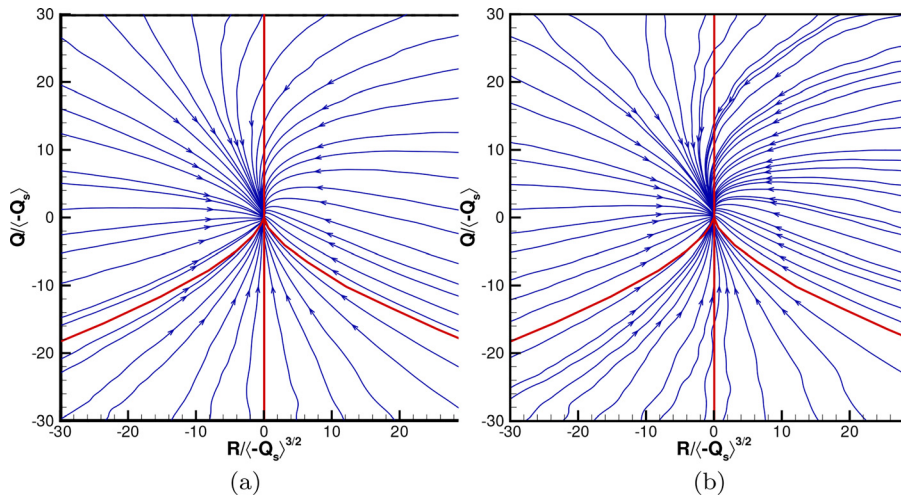


FIG. 14. CMT of VGT viscous dynamics obtained for (a) VoF and (b) IBM at the QS_3 station.

the origin of the (Q, R) phase space by reducing the VGT magnitude. The cumulative effect is that the preference for enstrophy production over strain production survives albeit with weak vorticity at the initial time and as a result the enstrophy starts to build up during the evolution making the fluid element evolve toward a state where its strain dominance is progressively reduced. Due to this, the element moves from the $(-Q, -R)$ quadrant to the $(+Q, -R)$ quadrant. At this quadrant, the element undergoes more vortex stretching, which in turn makes the fluid element more dominating in vorticity. However, the vortex stretching cannot increase forever as the vortex stretching acts as a sink and the increase in stretching weakens strain which in turn weakens the vortex stretching itself. Therefore, at some time, the dominion of enstrophy production over strain production stops. At this point, the fluid element has more vorticity and less strain. Since the vortex stretching has reached its plateau, whatever the small amount of strain available, it starts interacting with itself to generate

more strain which leads to strain production exceeding the enstrophy production making the third VGT invariant positive. As a result, the fluid element now finds itself in the $(+Q, +R)$ quadrant. The mechanism explained for inertial dynamics happen here. Eventually, the fluid element is brought to the right-hand side of the $D=0$ line. At this point, the pressure dynamics kick in to oppose the inertial dynamics and do not allow the strain production and strain to grow indefinitely. Thus, the sign of the third invariant starts changing once the fluid element evolves to the right-hand branch of $D=0$. Then, the cyclic process continues. Although the cyclic nature of CMTs gives an impression that the magnitude of VGT continually decreases to zero with an increase in time, we must be aware that the CMTs are time-averaged quantities. This means that the instantaneous values of time derivatives of Q and R are largely non-zero values but the time-averaged conditioned values are zero. This has been proven by Elsinga and Marusic.³⁷

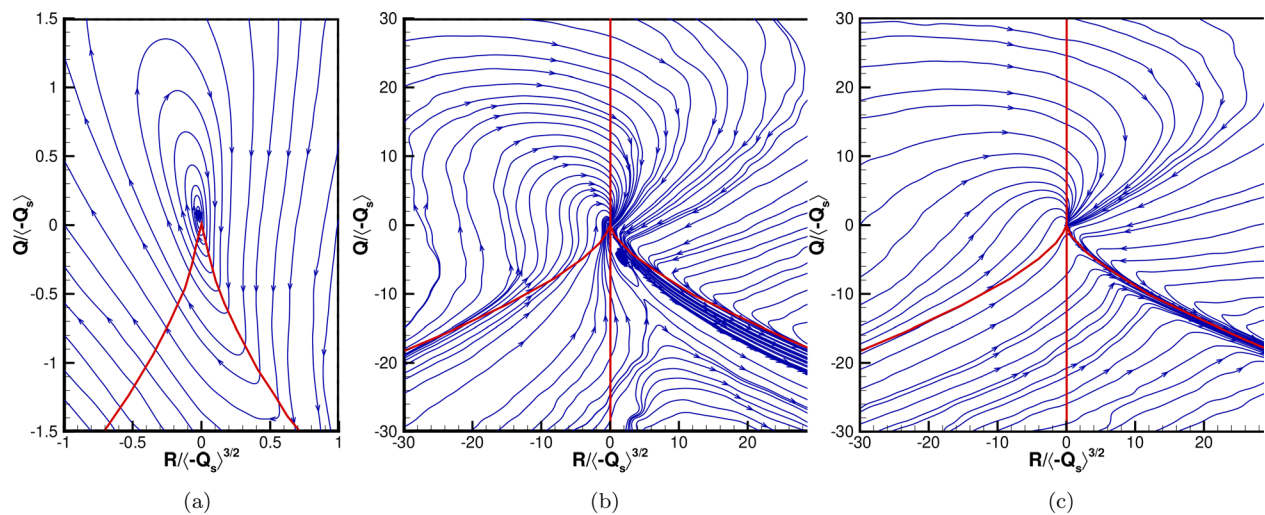


FIG. 15. CMT of VGT overall dynamics obtained for (a) HIT, (b) VoF, and (c) IBM. The BIT sub-figures are plotted for the US_3 station.

TABLE V. Values of $M(\dot{Q}, \dot{R})$ for BIT and HIT.

Simulation	$M(\dot{Q}, \dot{R})$
HIT	1.4
BIT/VoF: US_{-3}	79.3
BIT/IBM: US_{-3}	78.5
BIT/VoF: QS_{-3}	18.9
BIT/IBM: QS_{-3}	18.8

The magnitudes of the overall dynamics are given in the first row of Table V. This value agrees well with the literature.^{36,37,46,47}

2. Bubble induced turbulence

Let us now focus on the overall VGT dynamics of BIT. We noted in Secs. IV C–IV E that the individual inertial, pressure, and viscous dynamics of BIT are qualitatively similar to that of HIT. We are in for a surprise for the overall VGT dynamics of BIT as Figs. 15(b) and 15(c) show that the bubbly VGT dynamics are completely different from that of the HIT. The important feature of bubbly VGT dynamics is the presence of both stable node and unstable saddle points in the phase space. The trajectories are no longer cyclic. Here, we see two kinds of scenarios. The first case is when we consider any fluid element in the $(-Q, -R)$ quadrant under the $D=0$ line, this element evolves to the state where the strain and its production increase strongly and the trajectories move toward the unstable node, which is located approximately at $(R, Q) = (2, -3)$. Note that these values of Q and R are non-dimensional values. Second, when we consider a fluid element in the $(+Q, -R)$ quadrant, this element also evolves toward the origin at $(R, Q) = (0, 0)$. A similar result was reported for the near field of the grid generated turbulence where the wakes from the grid bars start meeting intermittently.³⁸ Here, in the case of BIT also, we have a flow that is dominated by the strain that is produced by non-local pressure. It appears that the inertial effects overcome the pressure dynamics when the strain in the fluid element is predominantly generated by the non-local pressure. In other words, the pressure dynamics effect becomes negligible in our case and in the case of turbulence generated by a fractal grid. In fact, the overall VGT dynamics of BIT in Figs. 15(b), 15(c), 17(a), and 17(b) look exactly same as the one predicted by the linear mean square estimation (LMSE)⁵¹ (see Fig. 2 in their paper) where the pressure Hessian term was neglected. Therefore, we postulate the following hypothesis. The role of pressure dynamics is indeed to oppose the inertial VGT dynamics of a fluid element. When the strain inside the fluid element is predominately generated by the non-local pressure, the pressure Hessian becomes ineffective in restricting the tendency to produce more enstrophy, the pressure dynamics should have helped this fluid element to oppose strain production and, thus, helped the fluid element to move diagonally upward in the (Q, R) phase space. In the BIT case, however, the strain inside the fluid element is already due to the pressure dynamics. As a result, the pressure dynamics decide not to oppose its own creation. Yet, there is the action of

viscosity acting as a damping term to make the fluid element move toward the origin. Thus, the fluid element continually moves toward the origin. As discussed for HIT, in reality, the velocity gradients magnitude would never be reduced to zero as the phase diagrams only represent the averaged values of the time derivatives of the second and third invariants of the VGT.

The above explanation can also be applied when the fluid element evolves to the right-hand branch of the $D=0$ line from the $(+Q, -R)$ quadrant. Here also, the pressure dynamics is strong but the strain inside the fluid element is already the result of the non-local pressure and as a result, the role of the pressure dynamics here seems to have reversed and it does not oppose the production of strain leading to fluid element moving upwards and evolving toward the unstable saddle.

Our theory can further be strengthened when we look at the combined dynamics of inertial and pressure effects on a fluid element. Such dynamics for HIT is shown in Fig. 16(a). We know that both inertial and pressure dynamics, when considered individually, would result in finite-time divergence as they continue to produce large velocity gradients. Therefore, the combination of pressure and inertial dynamics also would be expected to exhibit finite-time divergence. We get this intuitive result as the CMTs in Fig. 16(a) originate at the origin, and they move away from the origin indefinitely. We see an equal tendency for the fluid element to diverge with more strain with its production (i.e., toward the right-hand side branch of the $D=0$ curve) and more vorticity with its production (i.e., toward the top left quadrant). The physics revealed in Fig. 16(a) informs us that the pressure and inertial effects oppose each other equally.

Although the individual dynamics of pressure and inertial VGT was observed to be the same with the HIT, the combination of them for BIT differs drastically as shown in Fig. 16(b), which depicts such a scenario in the VoF simulation at the US_{-3} station. The most striking difference is that only a very few CMTs originate from the origin and such CMTs eventually get attracted to the unstable saddle in the $D=0$ line. For other CMTs, they look much similar to that of the inertial dynamics as they do not originate at the origin and they all move toward a state where strain and its production is more preferred and, thus, these CMTs continue to align along the $D=0$ line as the fluid element evolves in time. Now the physics is clear. The pressure dynamics for BIT, albeit strong, do not perform their classical work as

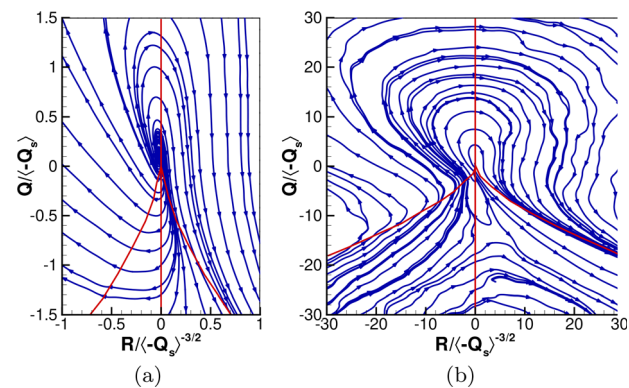


FIG. 16. CMT of VGT inertial and pressure dynamics obtained for (a) HIT and (b) VoF at the US_{-3} station.

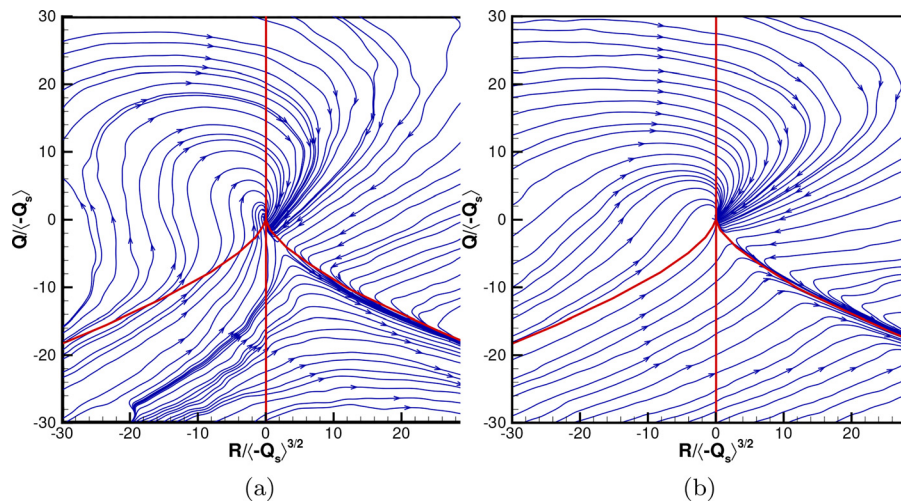


FIG. 17. CMT of VGT overall dynamics obtained for (a) VoF and (b) IBM at the QS_{-3} station.

in the case of HIT. This is one of the important findings of this paper, and this has huge ramifications for future studies.

In the case of multiscale grid turbulence, the non-cyclic behavior disappeared once the wakes from the grid bars are fully met and the turbulence is decaying. Therefore, we wanted to check if the observed non-cyclic behavior in BIT disappears for a longer time. This is the exact reason why we have been looking at stations QS_{-3} and US_{-3} throughout the paper. The overall VGT dynamics of BIT at the QS_{-3} station are given in Fig. 17. We see that the overall VGT dynamics do not change from US_{-3} to QS_{-3} albeit that the flow at the station QS_{-3} is fully developed and the bubble wakes are fully mixed. Yet, the flow keeps the memory from which it evolved even at the small scales rendering non-cyclic behavior in the overall VGT dynamics.

When we compare Figs. 15(b) and 15(c), we note that the bubble topology, breakup, and coalescence play no role in determining the overall VGT dynamics as both VoF and IBM produce the same results. This is further evidenced by the magnitude of overall VGT dynamics presented in the second and third rows of Table V where values obtained from VoF and IBM are similar. The table also ascertains our previous observation that the strength of the VGT dynamics of BIT is strong as we observe large values.

At the station QS_{-3} also, we see that the bubble deformation does not affect the overall VGT dynamics as Figs. 17(a) and 17(b) are nearly indistinguishable. This bolsters one of our important claims that we do not have to worry about modeling the breakup and coalescence if our main interest is about studying the fine-scale dynamics of BIT.

V. SUMMARY AND CONCLUSIONS

We studied the effect of bubble topology, breakup, and coalescence on the dynamics of velocity gradient tensor using numerical simulations. We used the volume of fluid to simulate bubbly turbulence, where the bubbles undergo breakup and coalescence and in the immersed boundary method simulation where the bubbles neither break up nor coalesce. We have also performed homogeneous isotropic turbulence simulation to validate the postprocessing subroutines we developed.

We observed that the energy spectra of VoF and IBM simulations exhibit a -3 slope for more than a decade of wavenumbers range. This result is consistent with the experimental findings. Since the flow is developing in nature, we considered two temporal locations for our study of fine-scale bubble turbulence dynamics. The first location is where the energy spectrum starts exhibiting a -3 slope. This location is also unsteady in nature. Thus, we called this location US_{-3} . Once the initial transients die out, the flow reaches a quasi-steady state with a -3 slope in the energy spectrum. We explored this temporal location as our second point of interest, and we called this location QS_{-3} .

To understand the fine-scale dynamics of bubble-induced turbulence, we looked at the VGT dynamics by tracing a single fluid element. This tracking is carried out using the conditional averaging method. The time-averaged values of time derivatives of the second and third invariants in the (Q, R) phase space yield conditional mean trajectory. We obtained CMTs by following a fluid element under the influence of individual dynamics, such as inertial, pressure, and viscous.

We found finite-time divergence of VGT dynamics when the fluid element is subject to inertial and pressure dynamics. The finite-time divergence in inertial dynamics is identified by the fluid element evolving toward a state of infinite strain and its production. On the contrary, the fluid element evolved toward a state of an infinite amount of vorticity and strain along with their productions when it is under the action of pressure dynamics. The viscosity acts on the fluid element to destroy the velocity gradients. These individual VGT term dynamics are consistent with the literature of HIT. Moreover, these results are the same irrespective of the location of temporal evolution (i.e., whether US_{-3} or QS_{-3}) and the simulation type (i.e., VoF or IBM). This shows that the bubble topology, breakup, and coalescence play no role in setting up fine-scale dynamics.

When we looked at the overall VGT dynamics of a fluid element, we observed an intriguing result for BIT. Although the individual terms of VGT dynamics are similar to that of HIT, the overall dynamics of BIT is entirely different from HIT. In HIT, the CMTs evolve cyclically toward the origin but we observed a non-cyclic behavior in BIT. After a careful analysis and gaining knowledge from relevant literature, we proposed that this difference is due to the nature of

pressure dynamics in BIT. Although the pressure dynamics oppose strain growing indefinitely in a fluid element, this action happens only when the strain is not due to pressure effects. That is why the pressure dynamics acts as a constraint for inertial dynamics whenever the amount of strain in a fluid element tries to increase toward infinity in the case of HIT. On the contrary, since most of the strain in BIT is due to non-local pressure, the pressure dynamics here fail to do their classical role to oppose the inertial dynamics. This results in non-cyclic behavior of overall dynamics in BIT. Interestingly, although the results of BIT and HIT differ for overall dynamics, both simulations (VOF and IBM) produce the same results meaning that bubble topology, breakup, and coalescence are negligible for the fine-scale BIT.

There are two important takeaways from this study. The fine-scale VGT dynamics of BIT is not the same as that of HIT. This means that we are in need of novel VGT models for bubbly flows. Second, we do not have to worry about bubble topology, bubble breakup, and coalesce when developing a fine-scale turbulence dynamics model for BIT. Although we have studied only one void fraction, the recent study by Mukherjee *et al.*⁵² reports that similar fine-scale turbulence characteristics can also be noted in void fractions as high as 45%. Therefore, the results presented in this study may be generalized for any void fraction, although further studies are needed to ascertain this.

ACKNOWLEDGMENTS

I.P. was supported by the Advanced Simulation and Computing (ASC) program of the US Department of Energy's National Nuclear Security Administration via the PSAAP-II Center at Stanford, Grant No. DE-NA0002373-1. M.S.D. acknowledges support from the Office of Naval Research (ONR), Grant No. N00014-15-1-2726. The authors acknowledge the Center for Turbulence Research (CTR) Summer Program which made this collaboration possible.

AUTHOR DECLARATIONS

Conflict of Interest

The authors have no conflicts to disclose.

DATA AVAILABILITY

The data that support the findings of this study are available from the corresponding author upon reasonable request.

APPENDIX: FURTHER DETAILS ON NUMERICAL METHODOLOGY

In this Appendix, we succinctly describe the numerical details of the two methods used to perform DNS. In both cases, a constant density ratio $\rho_b/\rho_l = 1.2 \times 10^{-3}$ has been adopted. The viscosity ratio, only relevant to VoF since IBM does not really solve the gas phase, is also a constant $\mu_b/\mu_l = 1.5 \times 10^{-3}$.

1. Volume of fluid (VoF) method

In the VoF method, the sharp interface between two immiscible fluids is determined using the VoF color function, C , which represents the volume fraction of the gas in each computational cell. We solve the governing equations, Eqs. (1a) and (1b), throughout

the whole computational domain, including the interior of the bubbles. The governing equations are discretized in space in an Eulerian framework using the second-order central difference scheme on a uniform staggered mesh.

A body force has been added in the direction of gravity to ensure that the net momentum flux in the vertical direction is zero (i.e., to prevent the uniform acceleration of both fluids). This modification has been used by other groups to simulate droplets and bubbles in periodic, vertical channels.^{16,53} In the VoF approach, the source term in Eq. (1b) is $\mathbf{f}_\sigma = \mathbf{f}_\sigma(\mathbf{x}, t)$, the surface tension force, which is computed by using Brackbill *et al.*'s continuum surface force approach,

$$\mathbf{f}_\sigma = \frac{\rho}{\bar{\rho}} \kappa \nabla C, \quad (\text{A1})$$

where $\bar{\rho} \equiv (\rho_l + \rho_b)/2$ and ρ_l and ρ_b are the water and air densities, respectively. The interface curvature κ is computed using the height-function method⁵⁴ with improvements developed by López *et al.*⁵⁵ The equations are integrated in time using the second-order Adams–Bashforth scheme, and the pressure is computed by solving Poisson equation for which a combination of a two-dimensional fast Fourier transforms (FFT) in the x - y plane and Gauss elimination in the z -direction⁵⁶ is used. This FFT-based method is 10–40 times faster than the standard multigrid-based pressure-correction method. Finally, we update the velocity field by applying pressure correction.

In our VoF method, the interface between the two fluids is reconstructed using a piecewise linear interface calculation.⁵⁷ The volume fraction C is advanced in time using the Eulerian implicit–Eulerian algebraic–Lagrangian explicit (EI–EA–LE) algorithm originally proposed by Scardovelli *et al.*⁵⁸ and later improved by Baraldi *et al.*⁵⁹ to ensure local and global mass conservation. Using the improved EI–EA–LE algorithm, the cell-centered volume fraction C is advected using the face-cent red velocity field \mathbf{u} . The method displays second-order spatial accuracy for values of Courant–Friedrichs–Lewy number ≤ 0.1 . Furthermore, the average geometrical error $[E_g = |C(\mathbf{x}) - C_{\text{exact}}(\mathbf{x})|]$ is less than 1% for a moving droplet with 30 grid cells or more across the diameter. The complete description of the method and the results are reported by Baraldi *et al.*⁵⁹ Breakup and coalescence of fluid volumes are handled implicitly by the VoF method. For example, if two interfaces occupy the same computational cell during the VoF update from time level n to $n + 1$, then the two VoF volumes are merged (or coalesced) automatically. Likewise, when the thickness of a bubble ligament falls below the grid spacing, h , it will break. It is worth mentioning here that these breakup and coalescence in VoF are not necessarily physical.

2. Immersed boundary method (IBM)

Rigid bubbles will be simulated using an Eulerian–Lagrangian code⁶⁰ with an implementation of the immersed boundary method (IBM).⁶¹ The liquid matrix, as stated before, is described by solving the Navier–Stokes equations; the diffusive and convective terms are discretized by second-order central difference schemes, whereas a three-step Runge–Kutta algorithm is adopted for the time derivatives. The solver is based on a predictor–corrector method in which a multigrid algorithm solves the Poisson equation for the pressure field. The dispersed phase—gas bubbles—are modeled as non-deformable

spheres. The gas–liquid interface of each bubble is comprised of a collection of N_L Lagrangian markers on which the coupling between frameworks is solved. This model does not account for breakup nor coalescence, assuming low void fractions and a significant presence of surfactant (“dirty” bubble). The motion of the bubble’s centroid is described by

$$m_b \frac{\partial \mathbf{u}_b}{\partial t} = \rho_l \int_S \mathbf{T} dS + (\rho_b - \rho_l) V_b \mathbf{g}, \quad (\text{A2})$$

where m_b is the bubble mass, $\mathbf{u}_b = \mathbf{u}_b(t)$ is the bubble centroid velocity, V_b is the bubble’s volume, \mathbf{g} is the gravity acceleration, and $\int_S \mathbf{T} dS = \int_S [-\frac{1}{\rho_l} \nabla p + \nu \nabla^2 \mathbf{u}] dS$ is the integral of the hydrodynamic stress tensor \mathbf{T} across the bubble’s surface. The latter is calculated by integrating for forces over all the Lagrangian markers at the bubble’s surface, following a similar procedure to Refs. 62 and 63.

At every time step, the position and velocity vectors for each bubble are distributed among the CPUs using a master-slave message passing interface (MPI)-based algorithm as described on Ouro *et al.*⁶⁴ Since the bubble is non-deformable, only the centroid’s properties are stored from one-time step to the next and the Lagrangian markers that constitute the surface are re-built depending on the prescribed diameter. A no-slip condition is forced upon the continuous phase velocity field at each one of the Lagrangians that define the surface. This starts by interpolating the liquid velocities at the exact location of the Lagrangian points using third-order delta functions⁶⁵

$$\mathbf{U}_L = \sum_{i=1}^{n_E} \tilde{\mathbf{u}}_i \cdot \delta(\mathbf{x}_i - \mathbf{X}_L) \Delta \mathbf{V}_E, \quad (\text{A3})$$

where \mathbf{U}_L is the interpolated liquid velocity at the point \mathbf{X}_L in Lagrangian coordinates, $\tilde{\mathbf{u}}$ is the undisturbed Eulerian velocity, \mathbf{x}_i is the Eulerian position vector, n_E is the number of Eulerian neighboring nodes, $\Delta \mathbf{V}_E$ is the cell volume, and δ is the interpolation delta function. Once the Eulerian velocities are mapped at the Lagrangian coordinates, the reaction force resulting from the no-slip condition is calculated explicitly through Eq. (A4) for every Lagrangian,

$$\mathbf{F}_L = \frac{\mathbf{u}_b^{t-1} - \mathbf{U}_L}{\Delta t}, \quad (\text{A4})$$

where \mathbf{u}_b^{t-1} is the bubble’s velocity at the previous time step. The hydrodynamic stress tensor $\int_S \mathbf{T} dS$ is obtained by integrating all the \mathbf{F}_L across all the Lagrangians defining the bubble’s interface. The forward coupling (liquid-to-bubble) is completed by calculating the resulting bubble velocity solving implicitly Eq. (A2). Once the bubble centroids’ positions are updated, the backward (bubble-to-liquid) coupling is achieved by calculating the forcing term \mathbf{f} at every Eulerian node within range (defined by the delta function’s stencil) of the bubble,

$$\mathbf{f}_i = \sum_{L=1}^{n_L} \frac{\mathbf{U}_L - \mathbf{u}_b^t}{\Delta t} \delta(\mathbf{X}_L - \mathbf{x}_i) \Delta V_L, \quad (\text{A5})$$

where \mathbf{f}_i is the contribution to the momentum balance of the Eulerian node i by n_L Lagrangian neighbors, Δt is the time step, and ΔV_L is the volume of influence of each Lagrangian marker. This

forcing term is used to correct the preliminary velocities before applying the multigrid solver, which will ensure mass conservation and provide the definitive Eulerian velocity field.

3. Homogeneous isotropic turbulence (HIT)

In the case of HIT, the forcing term in Eq. (1b) is a large-scale forcing term. We use the reduced-communication forcing (RCF), introduced by Onishi *et al.*,⁶⁶ to simulate the HIT. Here, the governing equations are discretized using the finite difference scheme. Then, a volume averaging is carried out which filters the small scales. These volume averaged velocities are transformed into spectral space, and they are forced in their large scales.

REFERENCES

- 1F. Risso, “Agitation, mixing, and transfers induced by bubbles,” *Annu. Rev. Fluid Mech.* **50**, 25–48 (2018).
- 2S. Elghobashi, “Direct numerical simulation of turbulent flows laden with droplets or bubbles,” *Annu. Rev. Fluid Mech.* **51**, 217–244 (2019).
- 3V. Mathai, D. Lohse, and C. Sun, “Bubbly and buoyant particle-laden turbulent flows,” *Annu. Rev. Condens. Matter Phys.* **11**, 529–559 (2020).
- 4G. Besagni, F. Inzoli, and T. Ziegenhein, “Two-phase bubble columns: A comprehensive review,” *Chem. Eng.* **2**, 13 (2018).
- 5M. Lance and J. Bataille, “Turbulence in the liquid phase of a uniform bubbly air–water flow,” *J. Fluid Mech.* **222**, 95–118 (1991).
- 6R. Zenit, D. L. Koch, and A. S. Sangani, “Measurements of the average properties of a suspension of bubbles rising in a vertical channel,” *J. Fluid Mech.* **429**, 307–342 (2001).
- 7F. Risso and K. Ellingsen, “Velocity fluctuations in a homogeneous dilute dispersion of high-Reynolds-number rising bubbles,” *J. Fluid Mech.* **453**, 395–410 (2002).
- 8J. Martínez-Mercado, C. A. Palacios-Morales, and R. Zenit, “Measurement of pseudoturbulence intensity in monodispersed bubbly liquids for $10 < \text{Re} < 500$,” *Phys. Fluids* **19**, 103302 (2007).
- 9G. Riboux, F. Risso, and D. Legendre, “Experimental characterization of the agitation generated by bubbles rising at high Reynolds number,” *J. Fluid Mech.* **643**, 509–539 (2010).
- 10S. Mendez-Diaz, J. Serrano-Garcia, R. Zenit, and J. Hernandez-Cordero, “Power spectral distributions of pseudo-turbulent bubbly flows,” *Phys. Fluids* **25**, 043303 (2013).
- 11V. N. Prakash, J. M. Mercado, L. van Wijngaarden, E. Mancilla, Y. Tagawa, D. Lohse, and C. Sun, “Energy spectra in turbulent bubbly flows,” *J. Fluid Mech.* **791**, 174–190 (2016).
- 12E. Alméras, V. Mathai, D. Lohse, and C. Sun, “Experimental investigation of the turbulence induced by a bubble swarm rising within incident turbulence,” *J. Fluid Mech.* **825**, 1091–1112 (2017).
- 13J. H. Lee, H. Kim, J. Lee, and H. Park, “Scale-wise analysis of upward turbulent bubbly flows: An experimental study,” *Phys. Fluids* **33**, 053316 (2021).
- 14F. Risso, “Theoretical model for k^{-3} spectra in dispersed multiphase flows,” *Phys. Fluids* **23**, 011701 (2011).
- 15B. Bunner and G. Tryggvason, “Direct numerical simulations of three-dimensional bubbly flows,” *Phys. Fluids* **11**, 1967–1969 (1999).
- 16B. Bunner and G. Tryggvason, “Dynamics of homogeneous bubbly flows Part 1. Rise velocity and microstructure of the bubbles,” *J. Fluid Mech.* **466**, 17–52 (2002).
- 17J. Lu and G. Tryggvason, “Numerical study of turbulent bubbly downflows in a vertical channel,” *Phys. Fluids* **18**, 103302 (2006).
- 18I. Roghair, J. M. Mercado, M. V. S. Annaland, H. Kuipers, C. Sun, and D. Lohse, “Energy spectra and bubble velocity distributions in pseudo-turbulence: Numerical simulations vs. experiments,” *Int. J. Multiphase Flow* **37**, 1093–1098 (2011).
- 19S. Dabiri, J. Lu, and G. Tryggvason, “Transition between regimes of a vertical channel bubbly upflow due to bubble deformability,” *Phys. Fluids* **25**, 102110 (2013).

- ²⁰J. Lu and G. Tryggvason, "Dynamics of nearly spherical bubbles in a turbulent channel upflow," *J. Fluid Mech.* **732**, 166–189 (2013).
- ²¹C. Santarelli and J. Fröhlich, "Direct numerical simulations of spherical bubbles in vertical turbulent channel flow," *Int. J. Multiphase Flow* **75**, 174–193 (2015).
- ²²C. C. Lai, B. Fraga, W. Chan, and M. S. Dodd, "Energy cascade in a homogeneous swarm of bubbles rising in a vertical channel," in *Annual Research Briefs* (Center for Turbulence Research, 2018), pp. 55–64.
- ²³V. Pandey, R. Ramadugu, and P. Perlekar, "Liquid velocity fluctuations and energy spectra in three-dimensional buoyancy-driven bubbly flows," *J. Fluid Mech.* **884**, R6 (2020).
- ²⁴A. Innocenti, A. Jaccod, S. Popinet, and S. Chibbaro, "Direct numerical simulation of bubble-induced turbulence," *J. Fluid Mech.* **918**, A23 (2021).
- ²⁵X. Zhang, J. Wang, and D. Wan, "Euler–Lagrange study of bubble drag reduction in turbulent channel flow and boundary layer flow," *Phys. Fluids* **32**, 027101 (2020).
- ²⁶X. Zhang, J. Wang, and D. Wan, "Euler–Lagrange study of bubble breakup and coalescence in a turbulent boundary layer for bubble drag reduction," *Phys. Fluids* **33**, 037105 (2021).
- ²⁷E. Trautner, M. Klein, F. Bräuer, and J. Hasslberger, "Conditional and unconditional second-order structure functions in bubbly channel flows of power-law fluids," *Phys. Fluids* **33**, 055121 (2021).
- ²⁸Y. Niida and Y. Watanabe, "Oxygen transfer from bubble-plumes," *Phys. Fluids* **30**, 107104 (2018).
- ²⁹E. Laurila, D. Izbassarov, M. Järvinen, and V. Vuorinen, "Numerical study of bubbly flow in a swirl atomizer," *Phys. Fluids* **32**, 122104 (2020).
- ³⁰A. Tsinober, *An Informal Conceptual Introduction to Turbulence* (Springer, 2009), Vol. 483.
- ³¹J. Hasslberger, M. Klein, and N. Chakraborty, "Flow topologies in bubble-induced turbulence: A direct numerical simulation analysis," *J. Fluid Mech.* **857**, 270–290 (2018).
- ³²M. S. Dodd and L. Jofre, "Small-scale flow topologies in decaying isotropic turbulence laden with finite-size droplets," *Phys. Rev. Fluids* **4**, 064303 (2019).
- ³³X. Chu, Y. Liu, W. Wang, G. Yang, B. Weigand, and H. Nematì, "Turbulence, pseudo-turbulence, and local flow topology in dispersed bubbly flow," *Phys. Fluids* **32**, 083310 (2020).
- ³⁴J. Hasslberger, P. Cifani, N. Chakraborty, and M. Klein, "A direct numerical simulation analysis of coherent structures in bubble-laden channel flows," *J. Fluid Mech.* **905**, A37 (2020).
- ³⁵J. Martìn, A. Ooi, M. S. Chong, and J. Soria, "Dynamics of the velocity gradient tensor invariants in isotropic turbulence," *Phys. Fluids* **10**, 2336–2346 (1998).
- ³⁶A. Ooi, J. Martìn, J. Soria, and M. S. Chong, "A study of the evolution and characteristics of the invariants of the velocity-gradient tensor in isotropic turbulence," *J. Fluid Mech.* **381**, 141–174 (1999).
- ³⁷G. Elsinga and I. Marusic, "Evolution and lifetimes of flow topology in a turbulent boundary layer," *Phys. Fluids* **22**, 015102 (2010).
- ³⁸Y. Zhou, K. Nagata, Y. Sakai, Y. Ito, and T. Hayase, "On the evolution of the invariants of the velocity gradient tensor in single-square-grid-generated turbulence," *Phys. Fluids* **27**, 075107 (2015).
- ³⁹E. Almèras, F. Risso, V. Roig, S. Cazin, C. Plais, and F. Augier, "Mixing by bubble-induced turbulence," *J. Fluid Mech.* **776**, 458–474 (2015).
- ⁴⁰D. Colombet, D. Legendre, F. Risso, A. Cockx, and P. Guiraud, "Dynamics and mass transfer of rising bubbles in a homogeneous swarm at large gas volume fraction," *J. Fluid Mech.* **763**, 254–285 (2015).
- ⁴¹S. Dabiri and G. Tryggvason, "Heat transfer in turbulent bubbly flow in vertical channels," *Chem. Eng. Sci.* **122**, 106–113 (2015).
- ⁴²M. S. Dodd and A. Ferrante, "A fast pressure-correction method for incompressible two-fluid flows," *J. Comput. Phys.* **273**, 416–434 (2014).
- ⁴³I. Paul and M. Dodd, "Fine-scale invariants in turbulence generated by rising bubbles," in *Annual Research Briefs* (Center for Turbulence Research, 2018), pp. 65–77.
- ⁴⁴M. S. Dodd, D. Mohaddes, A. Ferrante, and M. Ihme, "Analysis of droplet evaporation in isotropic turbulence through droplet-resolved DNS," *Int. J. Heat Mass Transfer* **172**, 121157 (2021).
- ⁴⁵P. Vieillefosse, "Local interaction between vorticity and shear in a perfect incompressible fluid," *J. Phys.* **43**, 837–842 (1982).
- ⁴⁶B. J. Cantwell, "Exact solution of a restricted Euler equation for the velocity gradient tensor," *Phys. Fluids* **4**, 782–793 (1992).
- ⁴⁷M. S. Chong, A. E. Perry, and B. J. Cantwell, "A general classification of three-dimensional flow fields," *Phys. Fluids* **2**, 765–777 (1990).
- ⁴⁸H. Tennekes and J. L. Lumley, *A First Course in Turbulence* (MIT Press, 1972).
- ⁴⁹I. Paul, G. Papadakis, and J. Vassilicos, "Genesis and evolution of velocity gradients in near-field spatially developing turbulence," *J. Fluid Mech.* **815**, 295–332 (2017).
- ⁵⁰I. Paul, G. Papadakis, and J. Vassilicos, "Direct numerical simulation of heat transfer from a cylinder immersed in the production and decay regions of grid-element turbulence," *J. Fluid Mech.* **847**, 452–488 (2018).
- ⁵¹J. Martìn and C. Dopazo, "Velocity gradient invariant evolution from a linear diffusion model," in *Proceedings of the Twelfth Australasian Fluid Mechanics Conference* (University of Sydney, 1995), pp. 743–746.
- ⁵²S. Mukherjee, A. Safdari, O. Shardt, S. Kenjeres, and H. E. Van den Akker, "Droplet–turbulence interactions and quasi-equilibrium dynamics in turbulent emulsions," *J. Fluid Mech.* **878**, 221–276 (2019).
- ⁵³D. Gueyffier, J. Li, A. Nadim, R. Scardovelli, and S. Zaleski, "Volume-of-fluid interface tracking with smoothed surface stress methods for three-dimensional flows," *J. Comput. Phys.* **152**, 423–456 (1999).
- ⁵⁴S. Cummins, M. Francois, and D. Kothe, "Estimating curvature from volume fractions," *Comput. Struct.* **83**, 425–434 (2005).
- ⁵⁵J. López, C. Zanzi, P. Gómez, R. Zamora, F. Faura, and J. Hernández, "An improved height function technique for computing interface curvature from volume fractions," *Comput. Methods Appl. Mech. Eng.* **198**, 2555–2564 (2009).
- ⁵⁶H. Schmidt, U. Schumann, and H. Volkert, "Three dimensional, direct and vectorized elliptic solvers for various boundary conditions," Report No. 84-15 (DFVLR-Mitt, 1984).
- ⁵⁷D. L. Youngs, "Time-dependent multi-material flow with large fluid distortion," *Numer. Methods Fluid Dyn.* **1**, 41–51 (1982).
- ⁵⁸R. Scardovelli, E. Aulisa, S. Manservigi, and V. Marra, "A marker-VOF algorithm for incompressible flows with interfaces," ASME Paper No. FEDSM2002-31241, 2002.
- ⁵⁹A. Baraldi, M. S. Dodd, and A. Ferrante, "A mass-conserving volume-of-fluid method: Volume tracking and droplet surface-tension in incompressible isotropic turbulence," *Comput. Fluids* **96**, 322–337 (2014).
- ⁶⁰B. Fraga, T. Stoesser, C. Lai, and S. Socolofsky, "A LES-based Eulerian–Lagrangian approach to predict the dynamics of bubble plumes," *Ocean Model.* **97**, 27–36 (2016).
- ⁶¹C. Peskin, "The immersed boundary method," *Acta Numer.* **11**, 479–517 (2002).
- ⁶²S. Schwarz, T. Kempe, and J. Fröhlich, "A temporal discretization scheme to compute the motion of light particles in viscous flows by an immersed boundary method," *J. Comput. Phys.* **281**, 591–613 (2015).
- ⁶³C. Santarelli and J. Fröhlich, "Direct numerical simulations of spherical bubbles in vertical turbulent channel flow. Influence of bubble size and bidispersity," *Int. J. Multiphase Flow* **81**, 27–45 (2016).
- ⁶⁴P. Ouro, B. Fraga, U. Lopez-Novoa, and T. Stoesser, "Scalability of an Eulerian–Lagrangian large-eddy simulation solver with hybrid MPI/OpenMP parallelisation," *Comput. Fluids* **179**, 123–136 (2019).
- ⁶⁵X. Yang, X. Zhang, Z. Li, and G. He, "A smoothing technique for discrete delta functions with application to immersed boundary method in moving boundary simulations," *J. Comput. Phys.* **228**, 7821–7836 (2009).
- ⁶⁶R. Onishi, Y. Baba, and K. Takahashi, "Large-scale forcing with less communication in finite-difference simulations of stationary isotropic turbulence," *J. Comput. Phys.* **230**, 4088–4099 (2011).
- ⁶⁷I. Paul, B. Fraga, M. S. Dodd, and C. C. K. Lai, "Role of breakup and coalescence in fine-scale bubble-induced turbulence. II. Kinematics," *Phys. Fluids* **34**, 083322 (2022).